Cerebral Cortex, June 2020;30: 3667–3685

doi: 10.1093/cercor/bhz334
Advance Access Publication Date: 20 February 2020
Original Article

ORIGINAL ARTICLE

Synaptic Mechanisms Underlying the Network State-Dependent Recruitment of VIP-Expressing Interneurons in the CA1 Hippocampus

Xiao Luo[1,2], Alexandre Guet-McCreight[3,4], Vincent Villette[1,2,6], Ruggiero Francavilla[1,2], Beatrice Marino[1,2], Simon Chamberland[1,2,7], Frances K. Skinner[3,5] and Lisa Topolnik[1,2]

[1]Department of Biochemistry, Microbiology and Bio-informatics, Laval University, Québec, PQ, Canada, [2]Neuroscience Axis, CHU de Québec Research Center (CHUL), Québec, PQ, Canada, [3]Krembil Research Institute, University Health Network, Toronto, ON, Canada, [4]Department of Physiology, University of Toronto, Toronto, ON, Canada, [5]Departments of Medicine (Neurology) and Physiology, University of Toronto, Toronto, ON, Canada, [6]Current address: Institut de Biologie de l'ÉcoleNormale Supérieure (IBENS), École Normale Supérieure, CNRS, INSERM, PSL Research University, Paris, France and [7]Current address: New York University Neuroscience Institute, New York, NY, USA

Address correspondence to Lisa Topolnik, Department of Biochemistry, Microbiology and Bio-informatics, Neuroscience Axis/CRCHUQ Research Center (CHUL), Laval University, Québec, Canada. Email: lisa.topolnik@bcm.ulaval.ca. Frances Skinner, Krembil Research Institute, University Health Network, Departments of Medicine (Neurology) and Physiology, University of Toronto, Toronto, Canada. Email: frances.skinner@gmail.com.
Authors Xiao Luo and Alexandre Guet-McCreight contributed equally to this work

Abstract

Disinhibition is a widespread circuit mechanism for information selection and transfer. In the hippocampus, disinhibition of principal cells is provided by the interneuron-specific interneurons that express the vasoactive intestinal polypeptide (VIP-IS) and innervate selectively inhibitory interneurons. By combining optophysiological experiments with computational models, we determined the impact of synaptic inputs onto the network state-dependent recruitment of VIP-IS cells. We found that VIP-IS cells fire spikes in response to both the Schaffer collateral and the temporoammonic pathway activation. Moreover, by integrating their intrinsic and synaptic properties into computational models, we predicted recruitment of these cells between the rising phase and peak of theta oscillation and during ripples. Two-photon Ca^{2+}-imaging in awake mice supported in part the theoretical predictions, revealing a significant speed modulation of VIP-IS cells and their preferential albeit delayed recruitment during theta-run epochs, with estimated firing at the rising phase and peak of the theta cycle. However, it also uncovered that VIP-IS cells are not activated during ripples. Thus, given the preferential theta-modulated firing of VIP-IS cells in awake hippocampus, we postulate that these cells may be important for information gating during spatial navigation and memory encoding.

Key words: calretinin, disinhibition, network oscillations, ripples, theta

Introduction

Spatial learning, formation of new memories and associated emotional context are encoded by the hippocampus (Andersen et al., 2007). This structure is populated by a high diversity of local-circuit and long-range projecting (LRP) GABAergic neurons, which play highly specialized roles in coordinating

different computations carried out by principal cells (PCs) (Soltesz 2006; Klausberger and Somogyi 2008; Pelkey et al. 2017). This is achieved through the cell type-specific and activity-dependent recruitment of different types of GABAergic neurons during distinct patterns of hippocampal network oscillations (Klausberger et al. 2003; Lapray et al. 2012; Varga et al. 2012; Katona et al. 2014). The mechanisms that may determine such network behavior of GABAergic cells have been the focus of intense investigation. From one side, the target-specific properties of the excitatory synapses that different types of inhibitory neurons receive may explain their distinct engagement during specific phases of network oscillations (Ali and Thomson 1998; Lei and McBain 2002; Losonczy et al. 2002; Pouille and Scanziani 2004; Glickfeld and Scanziani 2006). Alternatively, specific inhibitory mechanisms may exist to coordinate selectively the activity of GABAergic neurons (Francavilla et al. 2015).

Indeed, in the CA1 hippocampus, the so-called interneuron-specific (IS) inhibitory interneurons are unique in providing synaptic inhibition exclusively to GABAergic neurons. The type 3 IS cells (IS3s) that co-express vasoactive intestinal polypeptide (VIP) and calretinin (CR) (Acsády et al. 1996a, 1996b; Gulyás et al. 1996) innervate preferentially the somatostatin-expressing (SOM+) *oriens lacunosum-moleculare* (OLM) interneurons (Chamberland et al. 2010; Tyan et al. 2014). The OLM cells are known to fire at the trough of theta oscillation, but can be silent during the sharp wave-associated ripples (SWRs) via yet unknown mechanisms (Klausberger et al. 2003; Lapray et al. 2012; Varga et al. 2012; Pangalos et al. 2013; Katona et al. 2014). By inhibiting distal and disinhibiting proximal dendrites of CA1 PCs, OLM cells have been considered essential for modulating the integration of the temporoammonic (TA) versus Schaffer collaterals (SC) inputs (Sik et al. 1995; Leão et al. 2012; Amilhon et al. 2015; Siwani et al. 2018), burst firing of PCs (Lovett-Barron et al. 2012; Royer et al. 2012) and generation of theta oscillations in vitro (Gillies et al. 2002; Gloveli et al. 2005; Chatzikalymniou and Skinner 2018) and in vivo in the ventral hippocampus (Mikulovic et al. 2018). Thus, given that synchronous activation of IS3 cells is capable of pacing the OLM interneuron activity at theta frequency (Tyan et al. 2014), the IS3 input to OLM cells may act as a gear mechanism providing for rhythmic gating of the SC versus TA inputs in the CA1 area. Whether the IS3 cells are recruited during different patterns of network oscillations in vivo, including the theta rhythm, and what can be the underlying synaptic mechanisms operating in these cells, remains however unknown.

Here, we found that IS3 cells are equally well recruited via both SC and TA inputs, and may fire preferentially between the rising phase and peak of theta oscillation. Furthermore, while recruitment of IS3 cells to theta oscillations is largely determined by their synaptic properties, additional inhibitory mechanisms could restrain their activation during ripples.

Materials and Methods

Mice

Four mouse lines of either sex were used in this study: VIP/enhanced green fluorescent protein (*Vip*-eGFP; RRID:MMRRC_031009-UCD), *Vip*-IRES-Cre (Jackson #010908; RRID:IMSR_JAX:010908), B6.Cg-*Gt(ROSA)26Sor*$^{tm9(CAG\text{-}tdTomato)Hze}$/J (Ai9-RCL-tdT), and *Vip*-IRES-Cre-Ai9 (or *Vip*-tdTomato). *Vip*-eGFP line [MMRRC strain #31009, STOCK Tg(Vip-EGFP) 37Gsat], in which eGFP was targeted selectively to VIP+ interneurons (Tyan et al. 2014), was purchased from the MMRRC facility at the University of California (Davis, CA). *Vip*-tdTomato line was generated by breeding *Vip*-IRES-Cre mice with the reporter line B6.Cg-Gt(ROSA)26Sortm9(CAG-tdTomato)Hze/J (Ai9; RRID:IMSR_JAX:007909), stock #007909, The Jackson Laboratory, Bar Harbor, ME, USA. All experiments were performed in accordance with animal welfare guidelines of the Animal Protection Committee of Université Laval and the Canadian Council on Animal Care.

Patch-clamp Recordings in Hippocampal Slices

Mice (P14–30) were deeply anaesthetized with isoflurane (2%) or ketamine–xylazine (10–1 mg/mL). Transverse hippocampal slices (300 µm) were obtained as described previously (Chamberland et al. 2010; Tyan et al. 2014; Francavilla et al. 2018), and transferred to the recording chamber continuously perfused with heated artificial cerebrospinal fluid (ACSF) solution (at 30–32 °C) containing (in mM): 124 NaCl, 2.5 KCl, 1.25 NaH_2PO_4, 26 $NaHCO_3$, 2 $MgSO_4$, 2 $CaCl_2$, and 10 glucose (290–310 mOsm/L, pH 7.4). eGFP- and tdTomato-expressing cells were identified using blue and green light illumination, respectively, at upright microscope (Nikon Eclipse FN1) equipped with 40×/0.8 NA objective. Two-photon images of eGFP and tdTomato cells in acute slices were acquired using a two-photon microscope (TCS SP5; Leica Microsystems) equipped with a 25× water-immersion objective (NA, 0.95) and coupled to the Ti:Sapphire laser (Chameleon Ultra II; coherent; >3 W, 140 fs pulses, 80 Hz repetition rate). Voltage-clamp recordings were conducted using a cesium (Cs^+)-based solution (in mM): 130 $CsMeSO_4$, 2 CsCl, 10 diNa-phosphocreatine, 10 HEPES, 4 ATP-Tris, 0.4 GTP-Tris, 0.3% biocytin, 2 QX-314, 0.1 spermine, pH 7.2–7.3, 280–290 mOsm/L. For current-clamp recordings, a potassium (K^+)-based intracellular solution was used, containing (in mM): 130 $KMeSO_4$, 2 $MgCl_2$, 10 diNa-10 HEPES, 4 ATP-Tris, 0.4 GTP-Tris, and 0.3% biocytin (Sigma), pH 7.2–7.3, 280–290 mOsm/L. In some experiments, the following pharmacological agents were used: gabazine (10 µM, Ascent Scientific, Cat:ab120042), CGP-55845 (2 µM, Abcam Biochemicals, Cat:ab120337), NBQX (12.5 µM, Abcam Biochemicals, Cat:ab120046), and D,L-AP5 (100 µM, Abcam Biochemicals, Cat:ab120271). Passive membrane properties were recorded immediately after cell membrane rupture, while active membrane properties were recorded in current-clamp mode in response to somatic current steps (from −200 to +800 pA, with a step of 50 pA). Spontaneous excitatory postsynaptic currents (sEPSCs) were acquired in voltage clamp at −70 mV in the presence of gabazine. Spontaneous inhibitory postsynaptic currents (sIPSCs) were recorded at the reversal potential for EPSCs (0 mV). For electrical stimulation, a bipolar stimulating electrode (tip diameter, 2–3 µm) made from quartz theta glass (O.D.: 1.2 mm; I.D.: 0.9 mm; Sutter instrument) was placed in the CA1 *stratum lacunosum-moleculare* (LM) or *radiatum* (RAD). The EPSCs were evoked by electrical stimulation (1–5 pulses, 5–40 Hz, pulse width 0.2 ms) every 30 s in intact slices or in slices with microcut surgical isolation of SC or TA inputs as described in Jarsky et al. (2005).

For paired recordings, two *Vip*-eGFP cells were recorded simultaneously: one in current-clamp (presynaptic cell) and the second in voltage-clamp (postsynaptic cell) mode. The presynaptic IS3 cell was held at −60 mV, while the postsynaptic IS3 cells – at 0 mV to record unitary IPSCs. To study the possible synaptic connection between the two cells, two APs were evoked in the presynaptic cell with brief current injection (0.8–1 nA,

2–3 ms). In case of synaptic connection, short-latency (< 5 ms) unitary IPSCs were detected in the postsynaptic cell.

The series resistance (Rser; initial value: 15–25 MΩ) was monitored throughout the experiments by applying a −5 mV voltage step at the end of each sweep. Recordings with changes in Rser > 15% were discarded from the analysis. Data acquisition (filtered at 2–3 kHz and digitized at 10 kHz; Digidata 1440, Molecular Devices) was performed using the Multiclamp 700B amplifier and the Clampex 10.5 software (Molecular Devices). All recorded cells were filled with biocytin and confirmed post hoc as IS3 cells. The morphology of selected cells was validated using 3D reconstruction in Neurolucida 8.26.2 (MBF Bioscience).

Two-Photon Glutamate Uncaging

For two-photon glutamate uncaging, Alexa Fluor-594 (20 µM) was included in the intracellular solution to visualize the cell morphology. The caged compound MNI-Glu (5 mM, Tocris, Cat:1490) was applied into the recording chamber. Local photolysis of caged glutamate was achieved by using a two-photon Ti:Sapphire laser tuned to 730 nm (laser power, 25–30 mW) and coupled to Leica TCS SP5 microscope equipped with a 40× (0.8 NA) water-immersion objective. The proximal (<50 µm from soma) or distal (>100 µm from soma) dendritic segments of different length (2–8 µm) were illuminated for 9 ms (the smallest photostimulation duration that can be achieved in *xyt*-mode with our two-photon system). The size of the uncaging region was increased gradually until an action potential (AP) was evoked (Chamberland et al. 2010). Uncaging-evoked EPSPs or APs were recorded in current-clamp mode. To avoid photodamage, the laser power did not exceed 40 mW, and the photostimulation trials were spaced by 30-s rest intervals. In the end of the experiment, two-photon Z-stacks of cell filled with Alexa Fluor-594 were acquired with laser tuned to 800 nm to visualize the cell morphology.

Stereotaxic Injections

The viral vector AAV1.Syn.Flex.GCaMP6f.WPRE.SV40 (RRID: Addgene_100833) was injected in the CA1 area of *Vip*-IRES-Cre mice to express GCaMP6f selectively in VIP+ interneurons. The viral vector was produced at the University of Pennsylvania Vector Core facility (University of Pennsylvania, PA, USA). For stereotaxic injection, mice were deeply anaesthetized with intraperitoneal injection of ketamine–xylasine mixture (100/10 mg kg^{-1}) and fixed in a stereotaxic frame (Kopf Instruments). Viral vector was delivered using a microprocessor-controlled nanoliter injector (Word Precision Instruments) according to the following coordinates: CA1 (two sites were injected): site 1: AP –2.0 mm, ML +1.6 mm, DV –1.3 mm; site 2: AP, −2.5, ML, +2.1, DV, −1.3 mm. Viral vector was injected with the speed of 1 µL/min. The total volume was 100 nL. The pipette was kept for 5 min after injection and then withdrawn slowly, and the scalp was sutured. Mice were treated with a postoperative pain killer buprenorphine (0.1 mg/kg; 48 h) for three consecutive days or buprenorphine slow release (0.1 mg/kg) once. Animals were allowed to recover for 7–10 days before the implantation of hippocampal imaging window.

In Vivo Two-Photon Ca^{2+}-Imaging in Awake Mice

Two-photon somatic Ca^{2+}-imaging of neuronal activity was performed simultaneously with contralateral local field potential (LFP) recording in head-fixed awake mice (P85–98; $n = 3$) running on a treadmill as described previously (Villette et al. 2017; Francavilla et al. 2018).

For two-photon somatic Ca^{2+}-imaging from hippocampal CA1 VIP+ neurons, one week after AAV1.Syn.Flex.GCaMP6f.WPRE.SV40 injection, the overlying cortex was removed and a glass-bottomed cannula was inserted on top of the dorsal hippocampus and secured with Kwik-Sil at the tissue interface and Superbond at the skull level (Dombeck et al. 2010). A single tungsten electrode (33 Ω–CM/F, California Fine Wire) for LFP recordings was implanted in the *stratum pyramidale* (PYR) of the contralateral CA1 region and a reference electrode was implanted above the cerebellum (Villette et al. 2017). The head plate was oriented medio-laterally at 7–13° using a four-axis micromanipulator (MX10L, Siskiyou) and fixed with several layers of Superbond and dental cement. Mice were allowed to recover for several days with postoperative pain killer treatment for three consecutive days (buprenorphine, 0.1 mg/kg; 48 h).

To fix the awake animal under the objective of two-photon microscope, the head plate was clamped to a custom-made *X*-*Y*-moveable metal frame containing a circular treadmill (Villette et al. 2017). The treadmill was equipped with lateral walls to increase animal contentment and coupled with an optical encoder allowing for synchronous acquisition of running speed and LFP signal. For habituation to head-restricted condition, animals were handled and head-fixed for 5–15 min twice per day for 3–5 consecutive days before beginning the experiments. During experiments, animals showed spontaneous alternations between two behavior states: immobility and walking-running periods. The LFP signal and animal running speed were acquired at a sampling frequency of 10 kHz using the DigiData 1440 (Molecular Devices), AM Systems amplifier, and the AxoScope software (v10.5, Molecular Devices). Two-photon imaging was performed using a Leica SP5 TCS two-photon system coupled with a Ti:Sapphire laser (Chameleon Ultra II, Coherent), tuned to 900 nm. A long-range water-immersion 25× objective (0.95 NA, 2.5 mm working distance) was used for fluorophore excitation and light collection to external photomultiplier tubes at 12 bits. Image series were acquired at axial resolution of 2 µm/pixel and temporal resolution of 48 images/s. For each cell recorded, two 5-min imaging sessions were acquired. For each animal, the total length of imaging did not exceed 1 h. After imaging session, animals were returned to home cage. Between animals, the treadmill was cleaned with tap water.

Immunohistochemistry and Morphological Analysis

For immunohistochemical analysis of molecular markers expressed in hippocampal CA1 VIP+ cells and post hoc identification (expression of CR) of IS3 cells imaged in vivo (Figs 5*H*–*J* and S9), animals were intracardially perfused with sucrose-based ACSF followed by 4% paraformaldehyde (PFA) and 20% picric acid in phosphate-buffered saline (PBS), then the brain was extracted and fixed in 4% PFA/picric PBS overnight at 4 °C. On the next day, fixed brains were embedded in 4% agar. Hippocampal sections (thickness, 40–70 µm) were obtained using a vibratome (VT1000; Leica Microsystems or PELCO EasySlicer) and stored in PB sodium azide (0.5 mg/mL) solution. Sections were permeabilized with 0.1–0.3% Triton X-100 in PBS and incubated in blocking solution containing 20% normal serum for 1 h. Then, sections were incubated with primary antibodies at 4 °C for 24–48 h. After that, sections were incubated with conjugated secondary antibodies for 2–

4 h, rinsed, and mounted on microscope slides. Confocal images were obtained using a Leica TCS SP5 imaging system or Zeiss slide scanner (Axio Scan.Z1) equipped with a 488-nm argon, a 543-nm HeNe, or a 633-nm HeNe lasers and a 20× (NA 0.8), a 40× (NA 1.4), or a 63× (NA 1.4) oil-immersion objectives. The primary antibodies used were chicken-GFP (1:1000; Aves Labs Inc., Cat: GFP-1020; RRID:AB_10000240), goat-CR (1:1000; Santa Cruz Biotechnology, Cat: sc-11 644; RRID:AB_634545), and rabbit-CCK (1:800; Sigma, Cat: C2581; RRID:AB_258806). The secondary antibodies used were: donkey anti-chicken Alexa Fluor-488 (1:1000, Jackson Immunoresearch, Cat: 703-545-155), donkey anti-goat Dylight-650 (1:250; Thermo scientific, Cat: SA5-10089), and donkey anti-rabbit Alexa Fluor-647 (1:250; Invitrogen, Cat: A31573).

For axonal bouton analysis in IS3 cells, 70-µm slices obtained from the *Vip*-eGFP mice were processed for eGFP and CR immunoreactivity, and IS3 cells were identified based on the co-expression of VIP (eGFP) and CR. Confocal Z-stacks were acquired using a 63× oil-immersion objective with a 0.2-µm step, and the VIP+, CR+, or VIP+/CR+ boutons contacting the IS3 cell somata or dendrite (distance: 10–100 µm from the soma) were identified and counted in every cell. In total, 20 cells from five mice were analyzed.

For post hoc morphological analysis, patched cells were filled with biocytin (0.6 mg/mL, Sigma) during patch-clamp recording. After recording, 300-µm slices were fixed in 4% PFA at 4 °C overnight. To reveal biocytin, the slices were permeabilized with 0.3% Triton X-100 and incubated at 4 °C with streptavidin-conjugated Alexa-488 (1:1000, Jackson Immunoresearch, Cat: 016-540-084) or Alexa-546 (1:1000, Invitrogen, Cat: S11225) in Trizma buffer. Z-stacks of biocytin-filled cells were acquired with a 1.5-µm step and merged for detailed reconstruction in Neurolucida.

Computational Model

The models used in this study (SDprox1 and SDprox2) were previously custom-built to simulate electrophysiological characteristics of IS3 cells (ModelDB accession #: 223031) (Guet-McCreight et al. 2016). Simulations and subsequent analyses of calcium (Ca^{2+}) imaging data were run interchangeably on a Macbook Pro (13 inch, mid 2012, MacOS Sierra 10.12.6; 2.5 GHz Intel Core i5; 8 GB 1600 MHz DDR3) and a Dell Optiplex 7010 (Ubuntu 18.04.3 LTS; 3.40 GHz Intel Core i7-3770; 16 GB 1600 MHz DIMM DDR3). Models were simulated in the NEURON 7.5 environment and results were plotted using customized Python 2.7.13 (Macbook Pro)/2.7.15 (Dell) and Matlab R2017b to R2019a scripts. Note that all code and scripts can be accessed online (synaptic optimization code: https://github.com/FKSkinnerLab/IS3-Cell-Model/tree/master/LayerSpecificInputTests; rhythmic input simulations code: https://github.com/FKSkinnerLab/IS3-Cell-Model/tree/master/RhythmTests). For more details on the models, please see Supplementary Materials.

Data Analysis

Data acquired in electrophysiological experiments was analyzed in Clampfit 10.5 (Molecular Devices) and Igor Pro 4.0 (WaveMetrics). For the analysis of the AP properties, the first AP evoked with a current step of +40 to +60 pA within 50 ms from the beginning of the current step was analyzed. The AP amplitude was measured from the threshold to the peak. The AP half-width was measured at the voltage level corresponding to the half of the AP amplitude. Input resistance (R_{in}) and capacitance (C_m) were obtained using a membrane test in Clampex (Molecular Devices). The membrane time constant (T) was measured off-line using an exponential fit of voltage response to a hyperpolarizing step of −100 pA. The failure rate of unitary IPSCs in paired recordings was calculated only from the response to the first AP generated in the presynaptic cell. Somatic area, dendritic length, and dendritic surface were generated automatically from the 3D reconstructions of recorded cells in Neurolucida 8.26.2.

For the analysis of animal behavior on the treadmill during in vivo experiments, spontaneous locomotion activity was defined as time points, where the instantaneous speed was greater than 1 cm/s. Immobility periods were defined as the times when the speed was less than 1 cm/s. The run epochs were defined as contiguous periods when the instantaneous speed was larger than 1 cm/s for a minimal time period of 3 s (221 epochs of mean duration 8.95 ± 0.47 s). To identify run-starts for plotting in Fig. 6B–D, only run epochs where the average speed was below 1 cm/s for the 5 s preceding them were selected ($N = 64$; 17/18 cells). Likewise, to identify run-stops, only run epochs where the average speed was below 1 cm/s in the 5 s following them were selected ($N = 69$; 18/18 cells). Stationary epochs were defined as contiguous periods when the instantaneous speed was smaller than 1 cm/s for a minimal time period of 3 s (556 epochs of mean duration 9.31 s ± 0.31 s).

The image analysis was performed off-line using Leica LAS, Igor Pro (Wavemetrics) and Matlab. For extraction of somatic Ca^{2+}-transients, a region of interest was drawn around individual somata to generate the relative fluorescence change (F) versus time trace. For the purposes of automating the analysis, the baseline fluorescence level (F_0) was taken to be the median of the Ca^{2+} signal. Somatic Ca^{2+}-transients were expressed as $\Delta F/F = (F–F_0)/F_0$ or $\Delta F/F = (F–F_0)/F_0$ x 100%. This analysis was performed for 18 different putative interneuron-specific type 3 (pIS3) cells, of which 14 were recorded across two independent imaging sessions (5 min each) separated by 1 min intervals, and four cells were recorded during one session. Analyses between the two sessions were pooled together for each cell. Cross-correlations were computed using Matlab's xcorr(____,'coeff') function.

To extract estimated spike times from Ca^{2+} events, we applied three different algorithms: DF/Dt, MLSpike, and ultra-fast accurate reconstruction of spiking activity (UFARSA). In all cases, we tuned the spike extraction algorithm parameters according to in vitro calibration experiments (Fig. 5F,G). The first method was custom written using Matlab, whereas the other two are previously developed algorithms available in Matlab (see Supplementary Table 1 for details). For the first method, we took the gradient of the Ca^{2+} signal (DF/Dt) (Jackson et al. 2016) and chose times where the DF/Dt trace had crossed a threshold value of 0.75 times the standard deviation of the DF/Dt trace for at least two time-steps. In addition, the Ca^{2+} signal itself needed to be greater its own median plus standard deviation during these same time steps. Second, we used the MLSpike algorithm (Deneux et al. 2016), which we tuned to be optimal for GCaMP6f data and the levels of noise seen in our recordings. To further optimize the accuracy for each Ca^{2+} trace, we used MLSpike's functions for estimating the noise levels. Compared with the other two methods, MLSpike performed best in distinguishing signals from noise and detecting the spikes' onsets (Fig. 5F,G). Third, we used the UFARSA algorithm (Rahmati et al. 2018). While this algorithm provided some spike time estimates, it often under-estimated the number of spikes compared with

other algorithms. It is to be noted that large variabilities can exist in the time courses and magnitudes of Ca^{2+} transients, even within a given cell type. Therefore, considering all technical challenges associated with spike extraction (i.e., poor time resolution, variability in noise level and Ca^{2+} event shapes), all available methods for spike extraction from Ca^{2+} imaging data cannot be considered as precise, which is why we decided to use three different algorithms to compare the data obtained. Ultimately, these methods were used to provide an estimate of spike phases relative to the theta rhythm, such that they could link back to the model predictions regarding the modulation of IS3 cells *via* CA3 and entorhinal cortex inputs during theta rhythm.

To compute the percent of normalized spikes, we first normalized the numbers of spikes by how much the animal spends in that state. For example, more time spent immobile, would mean a smaller normalized number of immobile spikes. This is meant to compensate for animals that spend a lot more time in one state, which could generate more extracted spikes in that state by chance.

$$\text{Norm.immobile spikes} = \#\text{Immobile spikes} * \left(\frac{\text{Total time}}{\text{Time spent immobile}}\right)$$

$$\text{Norm.mobile spikes} = \#\text{Mobile spikes} * \left(\frac{\text{Total time}}{\text{Time spent mobile}}\right)$$

We then calculated the percent of normalized spikes (i.e., mobile vs. immobile) as follows:

$$\text{Immobile\% norm .spikes} = 100 \times \left(\frac{\text{Norm.immobile spikes}}{\text{Norm.immobile spikes} + \text{Norm.mobile spikes}}\right)$$

$$\text{Mobile\% norm .spikes} = 100 \times \left(\frac{\text{Norm.mobile spikes}}{\text{Norm.immobile spikes} + \text{Norm.mobile spikes}}\right)$$

To examine somatic Ca^{2+}-fluctuations in relation to network oscillations, LFP traces were band-pass filtered in the forward and reverse directions to obtain theta-filtered (5–12 Hz, fourth order) or ripples-filtered (125–250 Hz, eighth order; see Supplemental file 1 for an example Matlab code) traces. The onset of the theta-run epoch, which was always associated with an increase in the theta power, was defined by the beginning of the locomotion period based on the animal speed trace acquired simultaneously with LFP. To examine the time-varying relationships with theta power, we extracted the maximum powers from the spectrograms of the theta-filtered LFP traces between 5 and 12 Hz (see Supplemental file 1 for an example Matlab code). We labeled periods, where the time-varying theta power was greater than its mean as periods of "high-theta activity." For obtaining spike phases from the estimated spike times, we took the Hilbert transform (i.e., Matlab's hilbert(____) function) of the theta-filtered LFP signal and interpolated the spike phases from this trace. In this case, we set 0° to the rising phase of the theta oscillation.

Ripple events were detected automatically using custom written Matlab code. Specifically, we computed the envelope of the ripple-filtered trace by taking the complex magnitude (abs(____)) of its Hilbert transform (hilbert(____)). We then set a threshold criterion to identify time periods, where the envelope was greater than its mean plus five times its standard deviation for at least 12.5 ms. We chose this criterion manually to ensure that ripple events were both large enough in amplitude and long enough in duration. These time periods were then marked as ripple periods.

Quantification and Statistical Analysis

Data were initially tested for normality using Shapiro–Wilk test. If data were normally distributed, standard parametric statistics such as one-way ANOVA were used ($^{*}P < 0.05$, $^{**}P < 0.01$, and $^{***}P < 0.001$) to evaluate statistical significance using SigmaPlot 12.5 (Systat Software, Inc.) or Statistica 6 (StatSoft) and Clampfit 10.5 (Molecular Devices). If data were not normally distributed, Dunn's test or Mann–Whitney test was used for comparisons of multiple groups. The data are presented as means ± SEM. The "*n*" numbers described in the results indicate the number of cells, unless specified.

Statistical significance of cross-correlations was evaluated by doing a structured reshuffling of 10-s segments of the speed traces or time-varying theta power traces to generate 1000 surrogate cross-correlation traces. Within this surrogate dataset, the 95th and 99th percentile traces were computed using Matlab's prctile(____) function, in order to evaluate whether the peak or zeroth cross-correlation magnitudes fell above these percentiles. We computed Pearson's linear correlation coefficient between the different spike rate estimates and Ca^{2+} signals using Matlab's corr(X, Y, 'Type', and 'Pearson') function. Note that this function was also used to compute Pearson's linear correlation coefficient between the Ca^{2+} signals and speed traces. For comparisons of percent of normalized numbers of spikes between immobile and mobile states, we used Matlab's ttest(x, y, 'Alpha', and ____) function and paired-sample *t*-tests. All circular statistical and descriptive measurements were computed using the CircStat toolbox in Matlab (see Supplementary Table 2). Significance of the non-uniformity of circular spike estimate distributions relative to theta phase were tested using Rayleigh's method (circ_rtest(____)), and directional circular statistics were calculated using V-tests (circ_vtest(____)). Mean theta-phase modulation of spike estimates were computed using the circular mean (circ_mean(____)) and measures of dispersion included the vector length (circ_r(____)) and the angular deviation (circ_std(____)).

Results

Synaptic Properties of IS3 Interneurons

We took advantage of two transgenic mouse lines (*Vip*-eGFP and Vip^{Cre}) that express enhanced green fluorescent protein (eGFP) or Cre recombinase in VIP-expressing (VIP+) interneurons (Fig. 1A). The Vip^{Cre} mice were crossed with a reporter Ai9 line to achieve the tdTomato expression in VIP+ cells (Madisen et al. 2010). Both mouse lines (*Vip*-eGFP and Vip^{Cre}) have been previously characterized in detail and validated for the expression of the reporter fluorescent proteins selectively in cells expressing VIP endogenously (Tyan et al. 2014; David and Topolnik 2017; Francavilla et al. 2018). Consistent with previous findings on VIP expression in hippocampal interneurons (Acsády et al. 1996a, 1996b), in both mouse lines, fluorescently-labeled cells were located throughout the CA1, with many of these having a vertical orientation that resembled the IS3 cell morphology (Fig. 1A)

(Chamberland et al. 2010; Tyan et al. 2014). Indeed, 48.8% of VIP+ interneurons in the CA1 area (375/683 cells, $n = 3$ *Vip*-eGFP mice; 319/739 cells, $n = 2$ *Vip*-tdTomato mice) were co-expressing CR (Fig. S1), consistent with the interneuron-specific type 3 (IS3) cell neurochemical profile (Acsády et al. 1996a, 1996b). The remainder were VIP+/CR– cells, including a sparsely distributed population of cholecystokinin-co-expressing (CCK+) basket cells [*oriens/alveus* (O/A): 15.2%, PYR: 10.2%, RAD: 25.8%, LM: 22.2% of total VIP+ interneuron number/layer; average data for two mouse lines; Fig. S1] (Somogyi et al. 2004).

We characterized the morphological and electrophysiological properties of VIP-IS cells by making targeted patch-clamp recordings from the CA1 VIP+ interneurons in slices from both mouse lines. The biocytin-filled VIP-IS cells included in this analysis ($n = 72$) had somata located predominantly in the RAD, vertical orientation of dendrites extending to the LM and an axon arborizing within the O/A (Fig. 1*H*), consistent with the IS3 cell morphology (Acsády et al. 1996a, 1996b; Chamberland et al. 2010; Tyan et al. 2014). These cells had a high input resistance, slow membrane time constant, broad APs, and regularly spiking or irregular firing pattern (Fig. S2). The IS3 cell membrane and morphological properties were similar between the two mouse lines (Fig. S2; except the membrane capacitance which was smaller in IS3 cells recorded in *Vip*-tdTomato mice, $P = 0.00098$; Mann–Whitney test), and both lines were used for studying their synaptic properties.

Spontaneous excitatory synaptic drive was very low in these cells (Fig. 1*B*), with an average frequency of sEPSCs of 0.07 ± 0.01 Hz ($n = 6$). In contrast, the frequency of sIPSCs was significantly higher (0.77 ± 0.03 Hz, $P = 0.002$; one-way ANOVA; $n = 13$), indicating that under basal conditions in slices, the IS3 cells receive a dominant inhibitory drive.

The laminar location and frequent monopolar orientation of IS3 cell dendrites (Fig. 1*H*) suggests that these cells may be preferentially driven via the SC and TA inputs from CA3 pyramidal cells and entorhinal cortex, respectively. Accordingly, electrical stimulation in the RAD to activate the SC input elicited kinetically fast and large amplitude EPSCs in IS3 cells (amplitude: 24.0 ± 3.8 pA, rise time: 1.0 ± 0.3 ms, decay time constant: 3.9 ± 1.0 ms; $n = 14$, Figs 1*C–D* and S3), which exhibited a linear current–voltage (*I–V*) relationship (Fig. 1*D*), in line with a major role of the GluA2-containing Ca^{2+}-impermeable AMPARs at SC-IS3 cell synapses. In contrast, stimulation within the LM to activate the TA input evoked slower and smaller amplitude EPSCs in IS3 cells (Figs 1*C,E* and S3; EPSC amplitude: 12.1 ± 1.2 pA, $P = 0.035$, rise time: 2.5 ± 0.3 ms, $P = 0.003$, decay time: 9.9 ± 1.7 ms, $P = 0.012$, $n = 9$ for TA-EPSCs, $n = 14$ for SC-EPSCs; one-way ANOVA). Importantly, evoked EPSCs exhibited similar input-specific properties in intact slices and in slices with surgical isolation of SC and TA inputs by micro-cuts at the LM or RAD level, respectively (Figs 1*C* and S3) (Jarsky et al. 2005), pointing to the isolated activation of SC and TA pathways in intact slices with our stimulation protocol. Depolarizing the membrane above −50 mV revealed a second slow component to the TA-EPSC (Fig. 1*E*), indicating that NMDA receptors (NMDARs) may be present at TA-IS3 cell synapses. Indeed, the *I–V* relationship of the fast EPSC component was linear, whereas that of the slow component was outwardly rectifying (Fig. 1*E*, left; $n = 13$), suggesting that NMDARs contribute to the TA pathway transmission. Blocking the AMPA receptors with NBQX (12.5 µM) removed the fast component (peak EPSC amplitude decrease to $13 \pm 5\%$ of control at −70 mV, $n = 10$; Fig. 1*E*, right), while application of AP5 (100 µM), an NMDAR antagonist, inhibited the slow component of TA-EPSCs (peak EPSC amplitude decrease to $23.2 \pm 5.9\%$ of control at −30 mV, $n = 7$; Fig. 1*E*, right). Together, these data point to the synapse-specific contribution of NMDARs in IS3 cells, in line with previous reports on the input-specific organization of excitation in other interneuron types (Lei and McBain 2002; Glickfeld and Scanziani 2006; Sambandan et al. 2010; Le Roux et al. 2013).

We next explored the spatial integration of SC and TA inputs by IS3 cells using two-photon glutamate uncaging along the IS3 dendrite to mimic the activation of different numbers of excitatory synapses (Fig. 1*F*). In hippocampal slices from *Vip*-eGFP mice, two-photon uncaging (730 nm, 9 ms) of MNI-glutamate (5 mM) along the IS3 dendrite (2–8 µm length) elicited EPSPs (Fig. 1*F*) that were completely abolished by the combination of AMPA and NMDA receptor antagonists (NBQX, 12.5 µM; AP5, 100 µM; $n = 3$, not shown). We then explored how many synapses were potentially required for triggering APs at SC versus TA inputs by uncaging glutamate on proximal (SC input, < 50 µm from the soma, $n = 6$) versus distal (TA input, > 100 µm from the soma, $n = 5$) dendritic segments of the increasing length. The data showed no difference in the dendritic length necessary to evoke an AP within proximal and distal dendritic segments (SC-IS3: 6.5 ± 0.1 µm; TA-IS3: 5.1 ± 0.1 µm; Fig. 1*F,G*; $P = 0.173$, one-way ANOVA). Using the anatomical data on the excitatory synapse density in CR+ dendrites (Gulyás et al. 1999), we calculated that 5–7 synapses will be sufficient for triggering an AP at SC and 4–5 synapses at TA-IS3 inputs due to the layer-specific synaptic densities (RAD: 8.5–10 synapses/10 µm; LM: 7.5 synapses/10 µm). Collectively, these results indicate that, when activated synchronously, clusters of ∼5 synapses at different dendritic locations will drive the IS3 cell firing. Moreover, IS3 cells were efficiently recruited via both SC and TA inputs during repetitive activity (Fig. S4*A–C*).

Next, to explore whether IS3 cells receive inhibitory inputs from other VIP+ and/or CR+ cells as reported previously based on the electron microscopy and morphological analysis in the rat CA1 hippocampal area (Acsády et al. 1996a, 1996b; Gulyás et al. 1999), we performed paired recordings between VIP+ cells in slices from *Vip*-eGFP mice. The results showed that IS3 cells were connected to each other via dendritically located synapses, with unitary IPSCs having a small amplitude (19.7 ± 5.5 pA) and high failure rate ($80.3 \pm 5.5\%$, $n = 4$ connected pairs/33 attempts, Fig. 2*A,B*). In addition, we visualized the VIP+, CR+, and VIP+/CR+ axonal boutons on IS3 cell somata (Fig. 2*C*, top; Fig. 2*D*, top) and proximal dendrites (Fig. 2*C*, bottom; Fig. 2*D*, bottom). Taken together, these data indicate that IS3 cells receive inhibitory inputs from other VIP+ and CR+ interneurons [e.g., CR+ type 1 IS (IS1) and VIP+ type 2 IS (IS2) cells], and are connected with each other. However, further experiments will be required to reveal all inhibitory inputs to IS3 cells and the synapse-specific properties of their inhibitory currents.

Synaptic Properties of IS3 Cells Predict their Phase-Specific Firing During Network Oscillations *In Vivo*

To predict the input-specific synaptic recruitment of IS3 cells, we took advantage of previously developed IS3 cell multi-compartment models (Guet-McCreight et al. 2016). Using experimental data for SC- and TA-EPSCs, as well as IPSCs, we fit the weights, rise, and decay times for excitatory and inhibitory synapses onto each dendritic compartment and extrapolated a linear distance-dependent weight rule to generate realistic

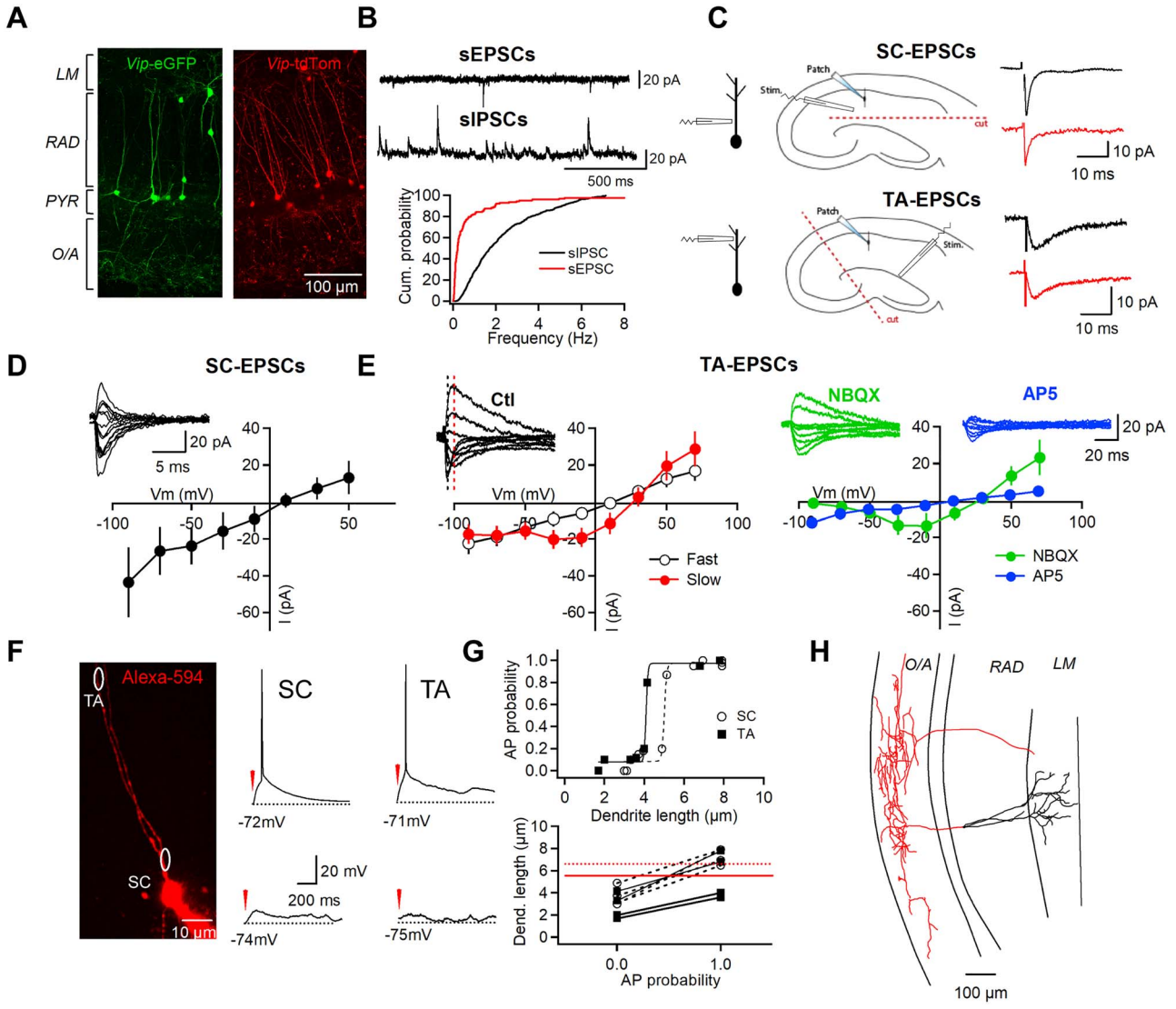

Figure 1. Synapse-specific properties and integration of excitatory inputs in IS3 cells. (*A*) Two-photon images of CA1 area in slices from *Vip*-eGFP (green) and *Vip*-tdTomato (red) mice. (*B*) Examples of recordings of sEPSCS and sIPSCs (top) and a summary cumulative distribution for sEPSC ($n = 6$) and sIPSC ($n = 13$) frequency (bottom). (*C*) Left, schematics illustrating the location of the stimulating electrode for SC (top) and TA (bottom) pathway activation; middle, schematics showing the location of surgical cut and stimulating/recording electrodes in slices with surgically isolated SC (top) and TA (bottom) inputs; right, example traces of EPSCs recorded in different cells at −70 mV in intact slices (black) and in slices with surgical cut (red). (*D*) Example traces of SC-EPSCs recorded at different voltage levels and summary *I–V* curve ($n = 5$). (*E*) Left, example traces of TA-EPSCs obtained at different voltage levels, with black and red vertical dotted lines indicating the peak levels for fast and slow EPSC components, respectively, and *I–V* curves of TA-EPSC fast (black) and slow (red) components ($n = 13$). Right, example traces of TA-EPSCs recorded in the presence of the AMPAR blocker NBQX (green) or the NMDAR antagonist AP5 (blue) with corresponding summary *I–V* relationships for the NMDAR ($n = 7$) and AMPAR ($n = 10$) components. (*F*) Left, two-photon image (single focal plane) showing the IS3 cell filled with Alexa-594 during recording and the location of the target areas in proximal (SC) and distal (TA) dendrites for two-photon glutamate uncaging. Right, Representative responses of IS3s when glutamate was released at shorter (bottom, 2–4 µm) and longer (top, 5–8 µm) dendritic areas at SC versus TA inputs. (*G*) Top, representative example of the AP probability in relation to photostimulation extends at two inputs. Bottom, summary data for a group of cells illustrating the transition to AP initiation when the length of stimulated dendrite was increased. Circles correspond to the SC and squares—to the TA inputs, respectively. Red lines indicate the mean threshold for dendritic length, at which it was possible to induce spikes at SC (dotted line) versus TA (continuous line) inputs. The difference in the dendritic length was not significant between the two inputs ($P = 0.173$; one-way ANOVA.) (*H*) Example of an IS3 cell (dendrites are shown in black, and axon in red) filled with biocytin in 300-µm slice and reconstructed in Neurolucida.

EPSCs and IPSCs across the entire dendritic arbor of the IS3 cell model (Fig. S5A). The weights used here predicted a biologically realistic range of receptors per synapse (Fig. S5B), and an increase in the measured reversal potential with distance from soma (Fig. S5C), which was in line with experimental observations (Fig. 1D,E). Using these realistic synaptic parameters, we simulated the in vivo-like conditions in the IS3 cell models—the model cells that were bombarded with excitatory and inhibitory synaptic inputs (Guet-McCreight and Skinner 2019). Briefly, these cell models included ion channels in soma only (*S*) as well as ion channels distributed in the soma and the first 70 µm of dendrites (i.e., somatodendritic; *SD*). These ion channel mechanisms included the transient sodium (G_{NaT}), persistent sodium (G_{NaP}), A-type potassium (G_{KA}), and delayed rectifier potassium (G_{KD}). We used two variant IS3 cell models with (SDprox1; $G_{NaT,SD}$: 0.07 S/cm^2, $G_{NaP,S}$: 0.000075 S/cm^2,

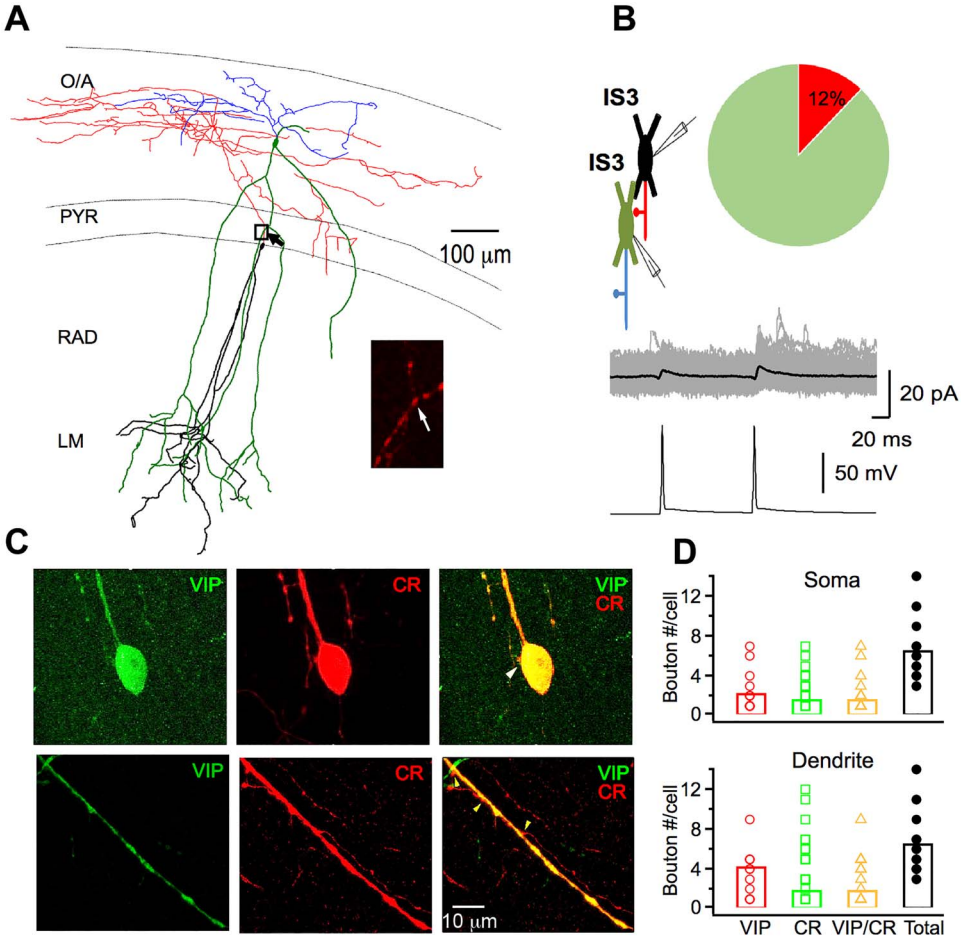

Figure 2. IS3 cells receive inhibitory inputs from VIP+ and CR+ interneurons. (*A*) Representative Neurolucida reconstruction (Z-stack from 300-µm slice) of the recorded connected pair of IS3 cells (the axons are shown in red and blue, while dendrites are shown in green and black), with an inset illustrating the axo-dendritic contact from the area indicated with a black square and an arrow in the reconstruction. (*B*) Schematic of the paired recording between two IS3 cells (top left), a summary pie-chart showing the connection ratio for IS3 cells (top right), and corresponding traces of unitary IPSCs (gray) with the averaged trace (black) in response to presynaptic APs (bottom). (*C*) Confocal image of the IS3 cell somata (top) and dendrite (bottom) identified based on the co-expression of VIP and CR, that receives VIP+/CR+ (somata) or CR+ (dendrite) axonal boutons indicated with yellow arrowheads. (*D*) Summary data showing the axonal bouton density (red – VIP+, green – CR+, orange VIP+/CR+, and black – the total number of boutons/cell) contacting the IS3 cell somata (top) and dendrites (bottom).

$G_{KA,SD}$: 0.07 S/cm^2, $G_{KD,SD}$: 0.025 S/cm^2; Figs 3 and 4) and without (SDprox2; $G_{NaT,SD}$: 0.055 S/cm^2, $G_{NaP,S}$: 0.00015 S/cm^2, $G_{KA,S}$: 0.03 S/cm^2, $G_{KD,SD}$: 0.295 S/cm^2; Fig. S7) dendritic A-type potassium channels, since the distribution of A-type potassium channels remains unknown in IS3 cells. Moreover, both model variants sufficiently captured the electrophysiology (i.e., back-propagating APs, and electrical regimes at four different current-step injections: hyperpolarization, subthreshold depolarization, spiking depolarization, and depolarization block) of IS3 cells (Guet-McCreight *et al.*, 2016).

We applied theta- and SWR-timed synaptic inputs to predict network state-dependent firing of IS3 cells in vivo. For theta-timed inputs in an in vivo-like scenario (Fig. 3), the phasic excitatory and inhibitory inputs spiked once per cycle (Fig. 3C), with a small amount of noise in their exact timing to enhance the model recruitment during theta-timed inputs (Fig. S6A). The model included different proximal and distal dendritic excitatory and inhibitory inputs based on their relative timing during theta oscillations recorded in CA1 PYR (Fig. 3A,B) (Klausberger and Somogyi 2008; Mizuseki et al. 2009). We found that both the SC- and TA-inputs could drive the phasic recruitment of the IS3 cell model (Fig. 3D–F), with the TA-input driving IS3 cell firing during the rising phase, and the SC-input—near the peak of the theta wave (Figs 3G,H and S6). Including proximal and distal inhibitory inputs at different phases of theta (i.e., the peak, the falling phase, and the trough), we found a significant reduction in the IS3 cell recruitment when any of the inhibitory inputs were doubled (Fig. 3H). Notably though, this effect was seen less with inhibitory inputs occurring near the falling phase and the trough of the theta cycle. Similar results were obtained with SDprox1 (Fig. 3) and SDprox2 (Fig. S7) IS3 cell models and, taken together, suggest that IS3 cells would spike between the rising phase and peak of the theta cycle in vivo.

For the SWR in vivo-like scenario (Varga et al. 2012; Katona et al. 2014), we first explored the impact of proximal excitatory inputs mimicking the SC-input from the CA3 PCs during SWR generation (Fig. 4A,B, left) (Frerking et al. 2005). We found that IS3 cells could exhibit an increase in activity above baseline when receiving a SC-input alone (Fig. 4C,D). However, including a delayed feed-forward inhibitory input onto the proximal

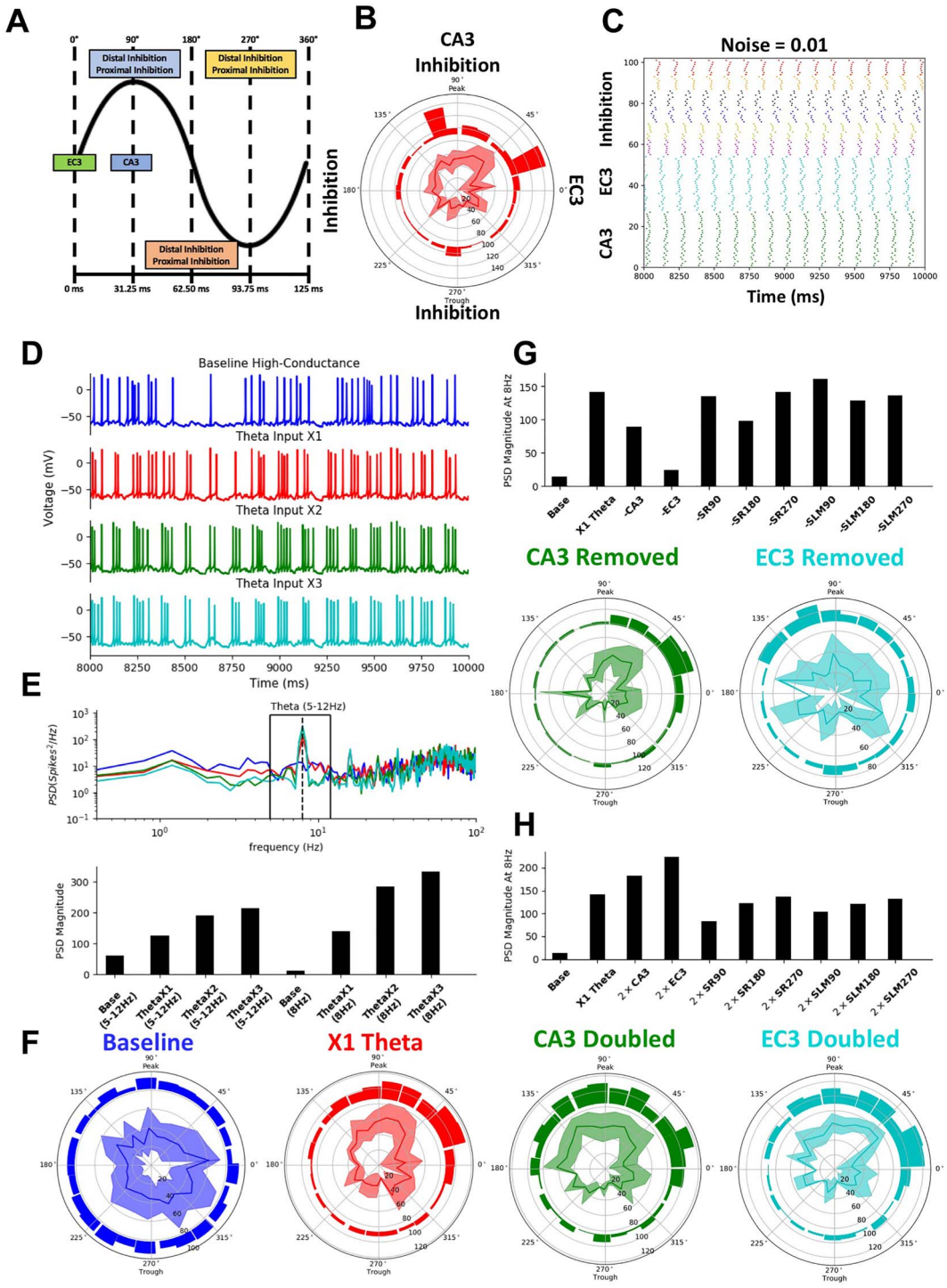

Figure 3. Model predicts firing of IS3 cells during the rising phase/peak of theta wave. (*A*) Relative timing of different theta-timed presynaptic populations (each different color in the boxes highlights inputs that are active at particular phases of theta). (*B*) Same as A, but in polar plot format with an example plot of the model phase preference when theta-inputs are perfectly timed. Inner traces show the mean frequencies of the interspike intervals, binned according to phase (binned standard deviations shown in the shaded areas). Outer histograms show the binned spike phases (bin width = 14.4°). (*C*) Example raster plot of the presynaptic theta-timed populations. (*D*) Example simulated voltage traces of resulting baseline in vivo-like conditions, X1 theta inputs, X2 theta inputs, and X3 theta inputs. (*E*) Top subplot: Power spectral density (PSD) of the IS3 cell model spike trains during baseline in vivo-like conditions, X1 theta inputs, X2 theta inputs, and X3 theta inputs. Bottom subplot: first four bars show the area under the PSD between 5 and 12 Hz, and the last four bars show the PSD magnitude at 8 Hz. (*F*) Polar plots showing phase preference of the IS3 cell model during theta-timed inputs. (*G*) Power spectral density (PSD) subplots at 8 Hz during removal of specified presynaptic theta-timed populations (top) and theta polar plots (bin width = 14.4°) predicting IS3 phase preference during removal of either CA3 or EC3 (bottom). SR90/SR180/SR270: stratum radiatum (i.e., proximal dendritic) inhibitory inputs at 90°, 180°, and 270°. SLM90/SLM180/SLM270: stratum lacunosum moleculare (i.e., distal dendritic) inhibitory inputs at 90°, 180°, and 270°. (*H*) Same as G, but with doubled presynaptic populations instead of removed.

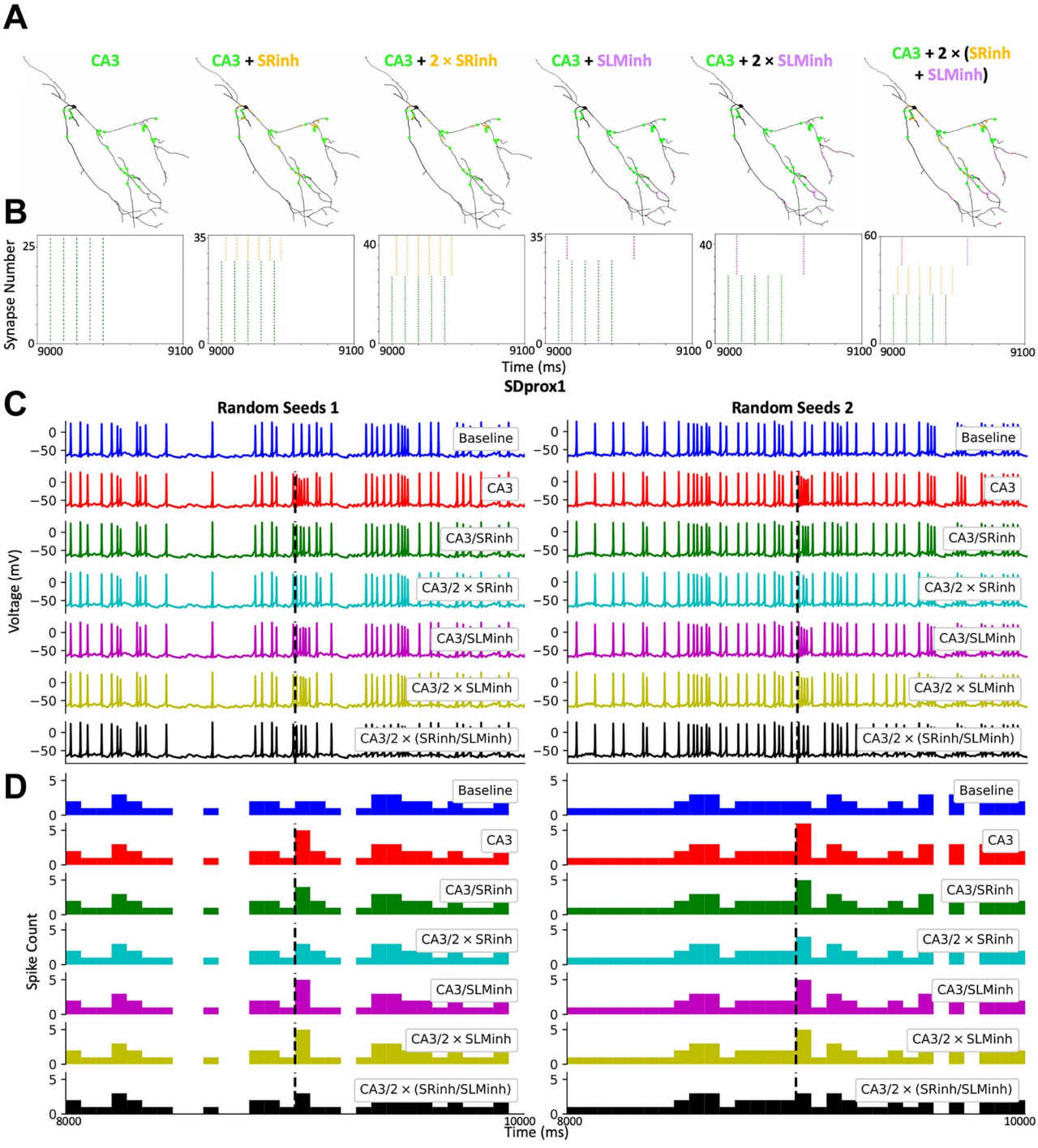

Figure 4. Local inhibitory inputs can dampen the IS3 cell recruitment during SWRs. (*A*) Example synaptic locations of SWR-timed inputs. Note that synaptic locations are chosen randomly in all simulations. (*B*) Raster plots of SWR-timed presynaptic populations. (*C*) Example voltage traces during SWR-timed inputs. Dashed black line coincides with the start of the SWR event. Note that we show two model examples, where we resample synaptic locations and baseline presynaptic spike times. (*D*) Peri-stimulus histograms corresponding to the voltage traces shown in C (bin size is 67 ms/30 bins). Note that delayed proximal inhibition is sufficient to bring the model spiking back to baseline levels. SRinh – proximal feedforward inhibition and SLMinh – distal feedforward inhibition.

(RADinh) or distal (SLMinh) dendrites, we found a substantial reduction in the IS3 cell recruitment. The impact of feedforward inhibition on the activity of IS3 cells was more prominent when RADinh and SLMinh inputs were combined (Fig. 4A–D, black). Similar results were obtained with SDprox1 (Fig. 4) and SDprox2 (Fig. S8) models, and when the synapse location and presynaptic spike timing were re-randomized (Figs 4 and 6; random seeds 1 vs. 2). Taken together, these results suggest that IS3 cells can spike during SWRs in response to the CA3 input. However, the activation of feed-forward inhibitory inputs converging onto

these cells (e.g., from other VIP+ or CR+ interneuron types) would have a strong dampening effect on their recruitment.

Delayed Recruitment of IS3 Cells During Theta-Run Epochs in Awake Mice

To test the model predictions, we next examined the recruitment of IS3 cells during different network states in vivo using two-photon calcium (Ca^{2+}) imaging in awake, head-restrained mice trained to run on the treadmill (Villette et al. 2017). We expressed a genetically-encoded Ca^{2+} indicator GCaMP6f (Chen et al. 2013) in VIP+ cells using a Cre-dependent viral vector AAV1.Syn.Flex.GCaMP6f.WPRE.SV40 injected into the CA1 area of Vip^{Cre} mice ($n = 3$ mice). Two-photon somatic Ca^{2+}-imaging was performed within the hippocampal CA1 PYR and RAD, the main location site of IS3 cell somata (Figs 1A, S1, and 5C), in combination with LFP recordings from the contralateral CA1 PYR (Fig. 5D, top) considering that theta oscillations are coherent between the two hemispheres, and SWRs occur simultaneously in left and right CA1 (Buzsáki et al. 2003; Malvache et al. 2016; Francavilla et al. 2018). In addition, recordings of the animal's speed were performed to track locomotion (Fig. 5A,B) and analyze hippocampal theta oscillations during theta-run episodes (speed > 1 cm/s; Fig. 5E, left) and SWRs during quiet states (speed < 1 cm/s; Fig. 5D, bottom and Fig. 5E, right) (Villette et al. 2017; Francavilla et al. 2019).

To estimate the firing onset in IS3 cells during different phases of network oscillations, we extracted the spike onset times from Ca^{2+} transients (CaTs) using three different algorithms (Fig. 5F). These included the Matlab toolboxes MLSpike (Deneux et al. 2016) and UFARSA (Rahmati et al. 2018), as well as a custom Matlab code estimating spike times using the speed of the Ca^{2+} signal (DF/Dt) (Jackson et al. 2016). The algorithms were first fine-tuned for IS3 cell-specific somatic CaTs using in vitro patch-clamp recordings of somatic CaTs in response to APs evoked by current pulse injection in anatomically confirmed IS3 cells (Fig. 5F,G). We found that, among the three algorithms tested, the MLSpike was the most accurate in distinguishing the signal from noise and estimating the spike time onset in IS3 cells (Fig. 5F,G).

In addition, to identify putative IS3 cells (pIS3s) within the population of VIP+ cells recorded in vivo, including the VIP+ basket cells (BCs), after in vivo imaging experiments, the brains were processed for immunolabeling for GFP and CR, the IS3 cell marker (Fig. 5H). The results showed that CR– and CR+ cells that were imaged within PYR/RAD separate well into two clusters due to a different soma size (Fig. 5I,J; CR+: $n = 17$; CR–: $n = 13$). In addition, the VIP+/CR– BCs were recognized based on their characteristic axonal pattern within the PYR, with basket-like branching that surrounded the putative soma of PCs (Fig. 5H, left, yellow arrowheads). These observations were confirmed by analyzing the soma parameters of IS3 cells and BCs derived from the anatomically reconstructed neurons recorded in vitro (Fig. S9; IS3: $n = 36$; BC: $n = 11$). The 3D rendering of somatic surface was used to develop the soma areas and extract the soma diameters in medio-lateral X- and rostro-caudal Y-dimensions from in vitro data (Fig. S9). Based on the data distribution for soma diameter and area in the anatomically confirmed IS3 cells and VIP+ BCs recorded in vitro (Fig. S9E), the cut-off parameters ($X \leq 16$ µm, $Y \leq 11$ µm, and soma area size ≤ 152 µm^2) were established to separate pIS3s from the putative BCs (pBC) in vivo (Fig. 5I,J). We then used these criteria to identify pIS3 and explore their activity during network states associated with locomotion and immobility (Fig. 6A,B, $n = 18$ cells, 221 running periods and 556 stationary states from two imaging sessions of 5 min each; see Methods for details).

Our data showed that, while the time-varying max theta power was significantly increased during run epochs (Fig. 6C), the CaTs were mainly observed during run-stop periods (Fig. 6D), pointing to the delayed recruitment of pIS3 cells during theta-run epochs. To further characterize this delay in CaTs, we calculated the cross-correlations of CaTs with running speed (Fig. 6E) and the time-varying theta power (Fig. 6F). Specifically, we looked at cross-correlation magnitudes at zero lags (i.e., zeroth peaks) between CaT, animal speed and LFP as well as their maximal peak magnitudes with corresponding lag times (Figs 6E,F and S10A–D). Significant zeroth peaks indicated a strong correlation between the CaTs and the running speed (Figs 6E and S10A,B) or CaTs and the theta power (Figs 6F and S10C,D). Similar positive relationships between the CaTs/estimated spikes and the animal speed (Fig. 6G) or CaTs/estimated spikes and the theta power (Fig. S10E) were obtained using Pearson's correlations. Furthermore, for both, the speed and the theta power, we found that, despite significant correlations between signals, most cells ($n = 15/18$ for speed; $n = 15/18$ for theta power) showed negative maximal peak lags (Fig. S10A–D), indicating that CaTs were delayed relative to the theta-run epoch onset. Importantly, in line with previous observations (Klausberger et al. 2003; Lapray et al. 2012; Varga et al. 2012; Katona et al. 2014), imaging somatic CaTs in CA1 O/A interneurons, which exhibit consistent phase-locked firing during theta oscillations, showed reliable recruitment of these cells during theta-run epochs, with zero lag between the CaT onset and change in the animal speed (Fig. S11; Francavilla et al. 2019), indicating that the delayed recruitment of pIS3 cells was not due to technical artifact. Together, these data indicate that while the activity of pIS3 cells correlates well with running speed and theta oscillation power, these cells exhibit a delayed recruitment.

IS3 Cells Prefer to Fire Near the Rising/Peak Phases of Theta Oscillations In Vivo

Given a strong correlation between the CaTs and the theta power (Fig. 6F), we next analyzed the theta-phase distribution of IS3 cell spiking, using the MLSpike algorithm for spike extraction and onset time estimates (Fig. 7A). We would like to note, however, that due to technical challenges associated with spike extraction from calcium signals (i.e., poor time resolution, variability in noise level, and Ca^{2+} event shapes), any given method for spike extraction from Ca^{2+} imaging data cannot be considered as precise. Nonetheless, we performed spike extraction from this data in order to provide a loose estimate of spike phases relative to the theta rhythm, and link back to the model predictions regarding the modulation of IS3 cells *via* CA3 and entorhinal cortex inputs during theta rhythm.

In line with significant correlation between the CaTs and the animal speed, the algorithm extracted a larger fraction of spikes during locomotion than during immobility in the majority of cells (Fig. 7B), highlighting a higher firing activity of pIS3 cells during locomotion. We then analyzed the theta-phase distribution of spikes during periods of running and high-theta activity. Pooling all of the spike phases from all cells together (Fig. 7C), we observed a significant non-uniform distribution ($P < 1e\text{-}11$, Rayleigh's tests) and a significant polarity toward the circular mean across all spike phases (see Supplementary Table 2;

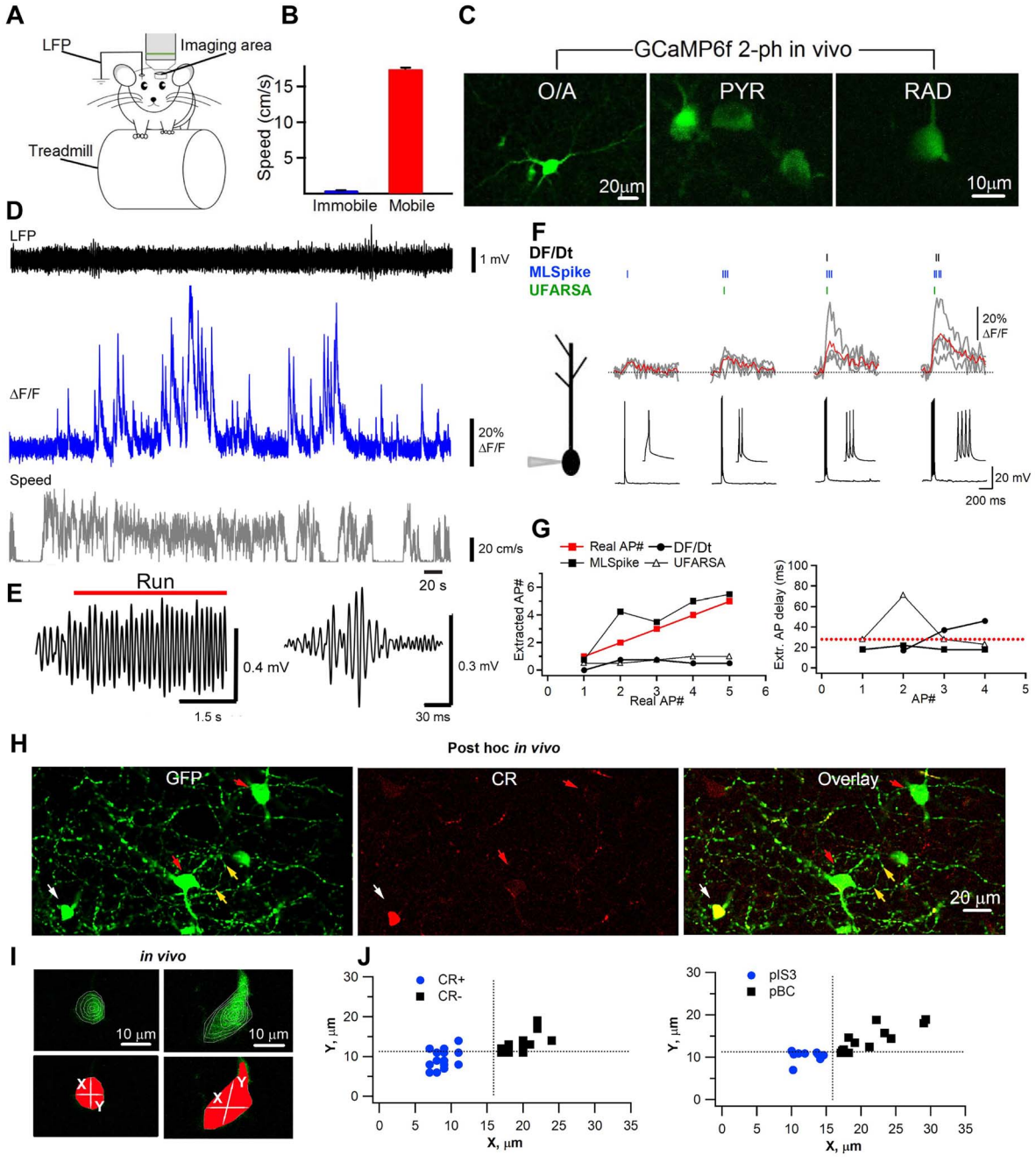

Figure 5. Imaging activity of pIS3 cells in awake mice. (*A*) Schematic of simultaneous Ca^{2+}-imaging and LFP recordings in awake mice. (*B*) Bar graph showing the average running speed during different behavioral states. (*C*) Representative two-photon images showing VIP+ cells located within O/A, PYR and RAD. Note a smaller size round somata of VIP+ cells within PYR and RAD. (*D*) Representative traces of simultaneous LFP recording (black) and somatic Ca^{2+} transients (blue) from a pIS3 cell during different behavioral states (gray trace: the higher animal speed during locomotion is reported as a high-frequency step pattern). The raw LFP signal was band-pass filtered in the forward and reverse directions (0.5–1000 Hz, eighth order). (*E*) Expanded theta-run period (left) and ripple event recorded during animal immobility (right). (*F*) Schematic of patch-clamp recording of GCaMP6f-expressing IS3 cell for in vitro calibration experiments (left) and average traces of somatic Ca^{2+} transients evoked in four different anatomically confirmed IS3 cells in response to different number of somatically evoked APs (right). Red traces correspond to intercell average Ca^{2+} transient. Small vertical lines on top of the Ca^{2+} transient traces indicate the spikes extracted with three different algorithms: DF/Dt (black), MLSpike (blue), and UFARSA (green). Note that MLSpike was the most accurate in predicting the spike appearance from somatic Ca^{2+} transients. (*G*) Left, summary graph showing the relationship between the number of extracted spikes and the number of real spikes. Right, the extracted spike delay as a function of spike number. Both graphs indicate that MLSpike algorithm showed the best performance in detecting the number of spikes and the time of their onset (red dotted line). (*H*) Representative confocal images of horizontal hippocampal sections processed for post hoc immunohistochemical identification following in vivo two-photon experiments illustrating the expression of GFP (GCaMP6f, left), CR (middle) and both (right). White arrowheads point to a VIP+/CR+ cell, red arrowhead—to VIP+/CR- putative basket cells, with an axon of one of them making the basket-like pattern (yellow arrowheads). (*I*) Two-photon raw (upper) and mask (lower) images of VIP interneurons recorded in vivo showing the extraction of somatic X- and Y- parameters for cell identification. (*J*) Summary data showing the clustering of in vivo recorded VIP cells based on the distribution of X- and Y- parameters (pIS3, blue; pBC, black). Dotted lines indicate the cut-off levels obtained from in vitro analysis and used for in vivo cell segregation (X = 15.9 μm, Y = 11.3 μm).

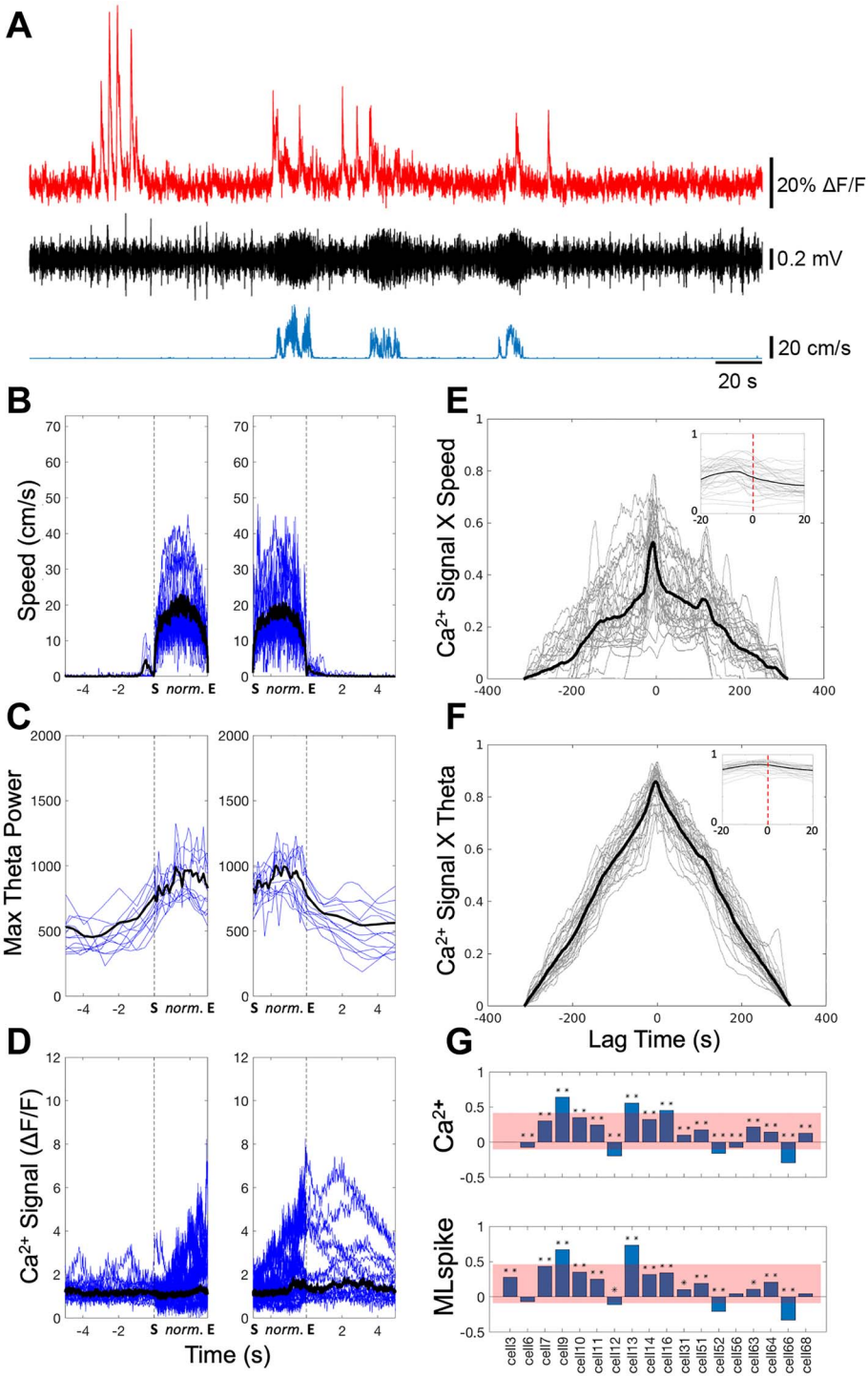

Figure 6. pIS3 cells are active during theta-run epochs. (*A*) Representative simultaneously recorded traces of a Ca^{2+} signal from a pIS3 cell (red), a theta-filtered (5–12 Hz) LFP recording (black), and animal speed (blue trace). (*B–D*) Average traces of speed (*B*), theta power (*C*), and Ca^{2+} signals (*D*) during run-starts (left panels; averages are across 64 run-starts selected across 17/18 cells) and run-stops (right panels; averages are across 69 run-stops selected across 18/18 cells). The vertical dashed lines show the transition into (left panels) or out of (right panels) run epochs. "S" denotes the start time of a run epoch, and "E" denotes the end time of a run epoch. For the run epoch portions in the time axes, the time vector is normalized (i.e., by using Matlab's interp1(_) function), such that the run epochs occupy the same span across the *x*-axis, despite having variable durations. The times outside of these run epochs are shown normally (i.e., ± 5 s pre- and post-run epochs). Blue lines show the mean traces for each cell. The mean of means across cells are shown in black, except for the Ca^{2+} signal in D, which shows the median of means. (*E–F*) Cross-correlations between the Ca^{2+} signal and speed (*E*), and the time-varying theta power (*F*). Average traces across all recordings are shown in black, and individual session traces are shown in gray. Speed cross-correlations (*E*) were quite variable but generally tended to exhibit large peaks near zero. Theta-filtered cross-correlations (*F*) also exhibited a mean large peak near zero. Inset plots show a zoomed in time scale of –20 s to 20 s (*Y*-axes are the same as the larger plots). (*G*) Pearson correlations of speed with either Ca^{2+} signal magnitude (top subplot), or MLSpike estimated spike rates (bottom subplot; $^{*}P < 0.05$; $^{**}P < 0.001$). Red area indicates the mean of Pearson correlations ± the standard deviation of Pearson correlations.

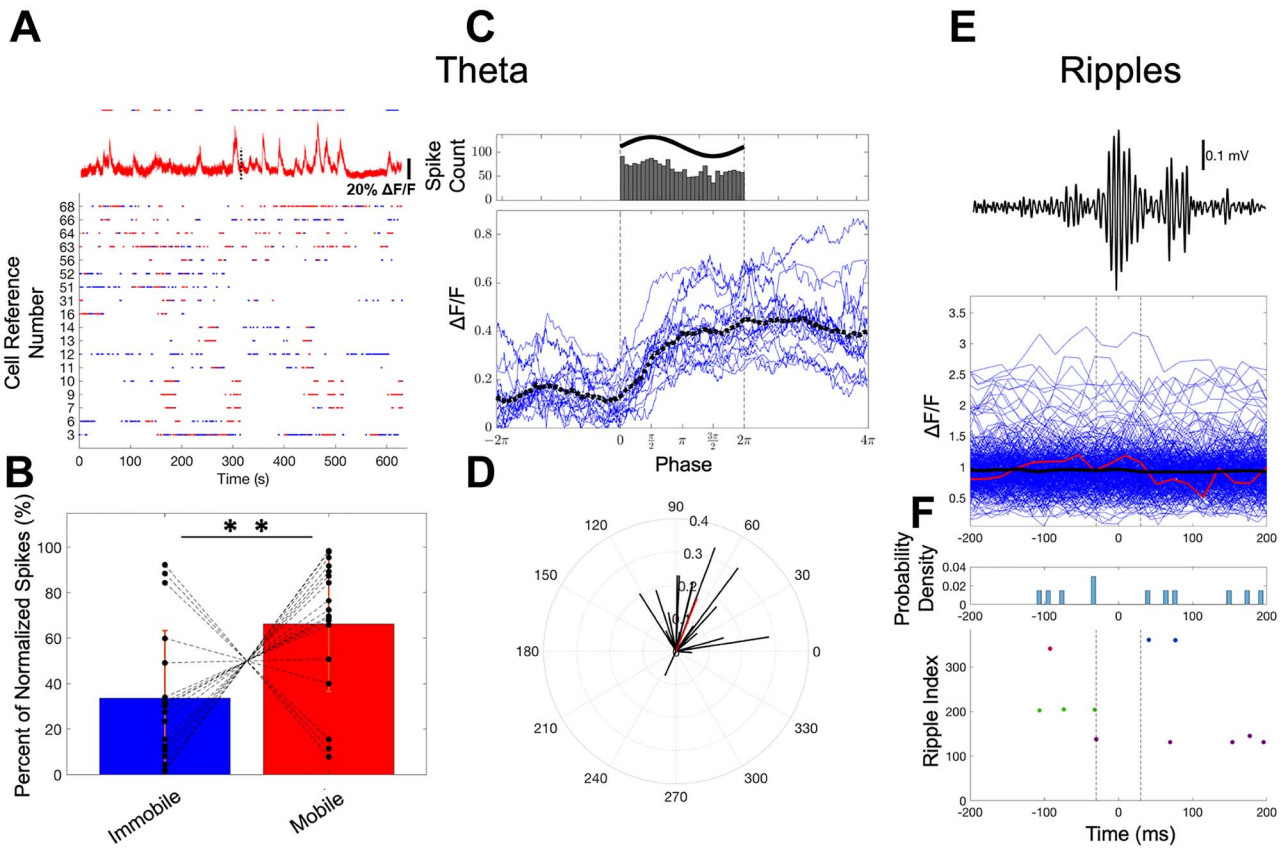

Figure 7. IS3 cells prefer to fire near the rising/peak phases of theta oscillation and are silent during ripples. (*A*) Raster plots for each cell, where blue dots are estimated spikes during immobile states, and red dots are estimated spikes during mobile states. Above the raster plot is a Ca^{2+} trace from cell #66, above which are the estimated spike extractions using the MLSpike algorithm. The dashed line in the Ca^{2+} traces indicates the time point where there was a 1 min break between recording sessions. (*B*) Percent of spikes for each state normalized relative to the states, where the animal was spending most of their time (statistical significance across states was evaluated using paired-sample *t*-tests). The dashed lines indicate which data points belong to the same cell (black dots). Bars indicate the mean, and the error bars indicate the standard deviation (**$P < 0.01$). (*C*) Top subplot: pooled distribution of theta-run spike phases (i.e., across all cells) relative to the theta-filtered LFP (bin width = $2\pi/30$). The theta cycle boundaries (i.e., 0–2π) are indicated by the vertical dashed lines. This pooled distribution was significantly non-uniform (Rayleigh's test), with a significant non-uniform polarity (V-test) toward the circular mean of the distribution (see Supplementary Table 1). Bottom subplot: medians of the calcium traces for each cell (blue lines) for segments of the calcium traces that align with theta cycles, where theta-run spikes were extracted using MLspike. Calcium trace segments are plotted against their corresponding theta phases. The theta cycle boundary (vertical dashed lines) is aligned with the boundary of the histogram in the upper subplot, and the medians the calcium traces of equal duration before (-2π) and after (4π) the theta cycle are also plotted. The dotted black line is the mean of medians across cells. Note that the minimal point in each raw calcium trace segment and then again in each median trace are aligned to 0 $\Delta F/F$, in order to ensure comparability across trace segments with different baselines. (*D*) Mean of means test. Each line shows the mean spike phase preference of a cell along the polar axis, where the vector length is shown along the radial axis. The red line indicates the mean of mean angles (i.e., polar axis) and the mean vector length (i.e., radial axis). This distribution was significantly non-uniform (Rayleigh's test), and had a significant polarity (V-test) toward the circular mean of the means (see Supplementary Table 1). (*E*) pIS3 cells are not active during SWRs. Peri-stimulus time histogram of all Ca^{2+} traces (blue lines) that occur during SWRs. The red line shows the Ca^{2+} trace that corresponds to the example SWR shown above the plot. The black line shows the mean across all Ca^{2+} traces. The dashed lines highlight the ±30 ms time window surrounding the SWR, which is centered at 0 ms along the time axis. (*F*) Peri-stimulus time histogram of the spike times estimated from the MLSpike algorithm. Note that the ripple index on the *y*-axis highlights how many ripples were analyzed, and the different dot colors corresponds to estimated spike times from different cells. Bin size in top subplots is 8 ms (i.e., 50 bins).

$P <$ 1e-12, V-tests). To characterize the dispersion of this distribution, we analyzed its vector length (vector lengths closer to one indicate higher clustering around the mean, i.e., less dispersion) and angular deviation (high values with a maximum of 81.03 indicate a large amount of dispersion). We found a vector length much smaller than one and angular deviations close to the maximal possible value of 81.03° (see Supplementary Table 2), indicating a broad distribution of spikes across theta phases. We also observed that calcium trace segments identified during theta cycles where theta-run spikes were extracted, on average tended to also have onsets aligned near the rising to peak phase of theta (Fig. 7C).

To further investigate this result, we performed the second-order analyses in which the mean of the mean angles across all cells was examined. For spike phase means, we found a significantly non-uniform distribution ($P <$ 1e-4, Rayleigh's test), as well as a significant mean spike phase preference with most vector lengths toward the rising/peak phase of the theta cycle ($P <$ 1e-5, V-test; Fig. 7D; see Supplementary Table 2). Similar results were obtained when using the UFARSA and DF/Dt spike extraction algorithms (see Supplementary Fig. S12 and Table 2) and are consistent with the model prediction that modulation from TA and SC pathways cause IS3 cells to fire preferentially during the rising phase and peak of the theta oscillation.

Finally, it has been reported that OLM interneurons, the main postsynaptic target of IS3 cells (Tyan et al. 2014), were often silenced during SWRs (Klausberger et al. 2003; Lapray et al. 2012; Varga et al. 2012; Katona et al. 2014), which, according to our model (Fig. 4), could result from the activation of IS3 cells via the SC input. However, the model also predicted that inhibitory inputs converging onto IS3 cells could dampen their recruitment during SWRs (Fig. 4C,D). Thus, to further expand upon theoretical predictions, we analyzed somatic CaTs recorded in pIS3 cells in relation to SWRs during immobility. Surprisingly, we did not observe any apparent CaTs that coincided with ripple episodes (Fig. 7E), indicating that IS3 cells are likely silent during ripples. Indeed, applying the MLSpike algorithm, out of the total number of spikes, we could only extract a few in relation to SWRs, and they were all preceding or following these events (Fig. 7F, bottom). Moreover, no change in the spike probability was observed during SWRs (Fig. 7F, top). Thus, as the model suggests, while IS3 cells can be driven via the SC pathway, activation of feedforward inhibitory inputs converging onto these cells may prevent their recruitment during SWRs.

Discussion

Here, we demonstrate that IS3 cells receive the TA and SC excitatory inputs with synapse-specific glutamate receptor composition. As a result, despite a different dendritic location, both TA- and SC-IS3 synapses were able to drive the IS3 cell firing when at least five closely spaced inputs were activated synchronously. Furthermore, these cells receive inhibitory inputs from the VIP+ and CR-expressing (CR+) CA1 interneurons, and are synaptically coupled to each other. Computational models of IS3 cells incorporating realistic synaptic conductances predicted their firing during the rising phase and peak of the theta cycle under in vivo-like conditions, with the SC and TA inputs providing the largest degree of modulation in terms of the spike timing of IS3 cells. During SWRs, the models predicted that CA3 input alone would be sufficient to recruit these cells, but activation of feedforward inhibition may dampen their activity. Two-photon Ca^{2+} imaging of pIS3 cells in awake mice revealed their delayed recruitment during theta-run episodes, with an estimated preferential firing at the rising phase/peak of the theta cycle as well as their silence during SWRs. Taken together, these data indicate that, while synaptic properties of IS3 cells determine in large their recruitment to network activity, additional inhibitory mechanisms may control the activity of these cells during specific network states. Of course, pIS3 cell silence during SWRs may also be due to simply not receiving excitation from CA3 during these states.

The TA versus SC pathway-specific synaptic transmission has been well characterized in PCs (Otmakhova et al. 2002; Arrigoni and Greene 2004). Compared with the SC synapses, those formed by the TA input exhibit slower currents and a higher NMDA/AMPA receptor ratio (Otmakhova et al. 2002). Similar to PCs, the distribution and subunit composition of postsynaptic glutamate receptors shows the input- and cell type-specific properties in hippocampal interneurons, with a profound impact on the input integration and induction of synaptic plasticity (Nyíri et al. 2003; Nissen et al. 2010; Camiré et al. 2012; Camiré and Topolnik 2012; Szabo et al. 2012). Specifically, the excitatory synaptic transmission at TA and SC pathways was compared in neurogliaform cells (Price et al. 2005), with NMDA and AMPA receptors being reported at both synapses. Our data indicate that TA-IS3 EPSCs have slower kinetics than SC-IS3 EPSCs, likely due to dendritic filtering, and are mediated in part by the activation of NMDARs. The AMPAR EPSC components of both TA- and SC-EPSCs showed linear current–voltage (*I–V*) relationships, indicating the expression of the Glu2A-containing AMPARs at both pathways. These data are consistent with the transcriptomic analysis of VIP+ neocortical (Paul et al. 2017) and hippocampal (Luo et al. 2019) GABAergic neurons, which revealed a highly enriched *Gria2* (GluA2 subunit) mRNAs in VIP+ cells. In addition, the *Grin2b* (GluN2B subunit) and *Grin2d* (GluN2D) transcripts were preferentially expressed in cortical VIP+ neurons (Paul et al. 2017; Luo et al. 2019). The high NMDA/AMPA receptor ratio controls dendritic spike initiation (Golding et al. 2002; Dudman et al. 2007; Brandalise et al. 2016) and may facilitate the recruitment of IS3 cells via TA input. Indeed, our data showed that a similar number of synchronously activated SC- or TA-synapses were required for eliciting APs in IS3 cells. It has been documented that the density of excitatory synapses on thick proximal dendrites of CR+ cells is 85.36/100 µm (0.85/µm), while on distal dendrites it is 75.31/100 µm (0.75/µm) (Gulyás et al. 1999). Accordingly, based on the dendritic length required to evoke a single AP in different dendritic microdomains (proximal: ~6.5 µm vs. distal: ~5.0 µm), the minimal number of synapses leading to the AP generation in IS3 cells may correspond to ~5 on proximal and ~4 synapses on distal dendrites. This observation indicates that additional mechanisms, such as increased NMDA/AMPA receptor ratio (Otmakhova et al. 2002), synaptic scaling of AMPARs (Magee and Cook 2000), or dendrite site-specific distribution of potassium channels (Guet-McCreight et al. 2016) may facilitate distal dendritic integration and spike initiation in IS3 cells.

Regarding the inhibitory inputs, we report that IS3 cells may be targeted by the other CA1 IS interneurons, including CR+ (IS1) and VIP+ (IS2) cells, and are connected to each other. These data are consistent with previous reports on the innervation of VIP+/CR+ cells by VIP+ or CR+ terminals in the rat CA1 hippocampus (Acsády et al. 1996b; Gulyás et al. 1996). While the strength of connection between IS3 cells was relatively weak, it may still play a role in the regulation of dendritic integration of excitatory inputs by IS3 cells and synchronization of their activity. Nevertheless, other CA1 interneuron types, such as SC and perforant pathway associated cells, may contact IS3 cells and provide more important inhibitory drive to these cells that may regulate their firing in vivo. In addition, it was shown that long-projecting medial septum GABAergic neurons make multiple synaptic contacts with hippocampal VIP+ cells (Papp et al. 1999) and may play a role in modulating IS3 cell activity during network oscillations (Dragoi et al. 1999; Hangya et al. 2009; Viney et al. 2013; Unal et al. 2015). Revealing the cellular identity of all IS3 modulators was beyond the scope of this study and will require new lines of investigation and combinatorial genetic strategies (He et al. 2016).

How can these synaptic mechanisms control the recruitment of IS3 cells during network oscillations in vivo? Using computational simulations, we demonstrate the impact of different excitatory and inhibitory inputs on IS3 cell firing. First, the relative timing and level of activity along the SC and TA pathways could define the spike timing of IS3 cells during theta oscillations. Second, removing inhibition of IS3 cells at the falling phase and trough of the theta wave could increase their firing, pointing to the importance of these phase-specific inputs for IS3 cell recruitment. In contrast, doubling inhibition, regardless of the theta phase, would decrease IS3 cell firing, indicating that strong inhibition can hinder the recruitment of these cells. Further-

more, in vivo Ca^{2+} imaging of pIS3 cells with estimated spike times was in line with the model predictions on the preferential firing of these cells during the rising phase/peak of the theta cycle, though with a large degree of phasic dispersion. Such high variability in the experimental data relative to the model could result from a number of factors including additional excitatory inputs that were not considered under the current study (e.g., CA1 PCs or subcortical neuronal populations), or cellular diversity within the pIS3 cell population. Indeed, we recently identified a new type of VIP+ LRP (VIP-LRP) cell in the CA1 hippocampus that, in addition to the CA1, innervates subiculum with a region-specific target preference (Francavilla et al. 2018). Further diversity was revealed within the VIP-LRP population, with cells co-expressing the muscarinic receptor 2, CR or proenkephalin in addition to VIP, and having somata located within PYR, RAD, or LM. Given that here the soma size of VIP+ cells recorded in vivo was used for pIS3 identification and that all CR+/VIP+ cells have a smaller soma size (Fig. 5I,J), the subiculum-projecting fraction of this population could be sampled as pIS3 cells and contribute to variability in cellular activity patterns. Indeed, we reported that the subiculum-projecting VIP+ cells are the theta-off cells, as they strongly decrease their activity during theta-run episodes (Francavilla et al. 2018). The latter was seen in a small number of pIS3 cells recorded in the current study (3/18 cells were decreasing activity during theta-run episodes) and may be due to specific modulatory inputs received by the two VIP+ cell types.

The model also predicted that IS3 cells would spike during SWRs driven by CA3 SC input, unless they receive a strong feed-forward inhibition. In line with the latter, we found no correlation between the pIS3 cell activity and SWR appearance in vivo. The mechanisms responsible for IS3 cell suppression during SWRs currently remain unclear but, in addition to local and long-range inhibition, may involve subcortical neuromodulatory projections. For example, serotonergic input from the median raphe nucleus was shown to modulate hippocampal SWRs (Wang et al. 2015), which may depend on the cell type-specific expression of specific types of 5-HT receptors. In addition to a well-documented expression of the excitatory 5-HTR3a by VIP+ cells (Lee et al. 2010; Rudy et al. 2011), recent transcriptomic analysis revealed several 5-HT receptor genes involved in the inhibitory signal transduction (e.g., *5Htr1a* and *5Htr1d*) (Luo et al. 2019). Whether these candidate receptors are expressed by IS3 cells and lead to suppression in their activity during ripples remains to be explored.

In conclusion, our data predict the preferential recruitment of IS3 cells during theta oscillations. As a result, a slow inhibition provided by these cells onto OLM cells via α5 $GABA_A$ receptor-containing synapses (Salesse et al. 2011; Magnin et al. 2019), which can pace OLM cell activity (Tyan et al. 2014) at theta frequencies, may be involved in the coordination of theta-oscillations (e.g., type II theta associated with the emotional context) (Mikulovic et al. 2018). Moreover, tuned by specific learning paradigms in relation to animal mood state and experience, such as reward (Pi et al. 2013) or goal-oriented behavior (Pinto and Dan 2015; Turi et al. 2019), IS3 cells may play the role of an important modulator of microcircuit activity for information selection and encoding.

Supplementary Material

Supplementary material is available at *Cerebral Cortex* online.

Funding

This work was supported by the Canadian Institutes of Health Research (CIHR) and the Natural Sciences and Engineering Research Council of Canada (NSERC). Vincent Villette was supported by the PDF fellowship from Savoy Foundation. Alexandre Guet-McCreight was supported by an NSERC CGS-D award.

Notes

We thank Sarah Côté and Stephanie Racine-Dorval for technical assistance and Dimitry Topolnik for equipment calibration and maintenance. Correspondence should be addressed to Dr Lisa Topolnik: lisa.topolnik@bcm.ulaval.ca and Dr. Frances Skinner: frances.skinner@gmail.com. *Conflict of Interest*: None declared.

References

Acsády L, Arabadzisz D, Freund TF. 1996a. Correlated morphological and neurochemical features identify different subsets of vasoactive intestinal polypeptide-immunoreactive interneurons in rat hippocampus. *Neuroscience*. 73:299–315.

Acsády L, Görcs TJ, Freund TF. 1996b. Different populations of vasoactive intestinal polypeptide-immunoreactive interneurons are specialized to control pyramidal cells or interneurons in the hippocampus. *Neuroscience*. 73:317–334.

Ali AB, Thomson AM. 1998. Facilitating pyramid to horizontal oriens-alveus interneurone inputs: Dual intracellular recordings in slices of rat hippocampus. *J Physiol*. 507: 185–199.

Amilhon B, Huh C, Manseau F, Ducharme G, Nichol H, Adamantidis A, Williams S. 2015. Parvalbumin interneurons of hippocampus tune population activity at theta frequency. *Neuron*. 86:1277–1289.

Andersen P, Morris R, Amaral D, Bliss T, O'Keefe J. 2007. *The Hippocampus Book*. Oxford Neuroscience Series, Oxford (New York): Oxford University Press: Oxford, UK.

Andrásfalvy B, Magee J. 2001. Distance-dependent increase in AMPA receptor number in the dendrites of adult hippocampal CA1 pyramidal neurons. *J Neurosci*. 21:9151–9159.

Antal M, Fukazawa Y, Eördögh M, Muszil D, Molnár E, Itakura M, Takahashi M, Shigemoto R. 2008. Numbers, densities, and Colocalization of AMPA- and NMDA-type glutamate receptors at individual synapses in the superficial spinal dorsal horn of rats. *J Neurosci*. 28:9692–9701.

Arrigoni E, Greene R. 2004. Schaffer collateral and perforant path inputs activate different subtypes of NMDA receptors on the same CA1 pyramidal cell. *Br J Pharmacol*. 142:317–322.

Brandalise F, Carta S, Helmchen F, Lisman J, Gerber U. 2016. Dendritic NMDA spikes are necessary for timing-dependent associative LTP in CA3 pyramidal cells. *Nat Commun*. 7:13480.

Buzsáki G, Buhl D, Harris K, Csicsvari J, Czéh B, Morozov A. 2003. Hippocampal network patterns of activity in the mouse. *Neuroscience*. 116:201–211.

Camiré O, Topolnik L. 2012. Functional compartmentalisation and regulation of postsynaptic Ca^{2+} transients in inhibitory interneurons. *Cell Calcium*. 52:339–346.

Camiré O, Lacaille J-C, Topolnik L. 2012. Dendritic signaling in inhibitory interneurons: Local tuning via group I metabotropic glutamate receptors. *Front Physiol*. 3:259.

Chamberland S, Salesse C, Topolnik D, Topolnik L. 2010. Synapse-specific inhibitory control of hippocampal feedback inhibitory circuit. *Front Cell Neurosci*. 4:130.

Chatzikalymniou A, Skinner F. 2018. Deciphering the contribution of Oriens-Lacunosum/Moleculare (OLM) cells to intrinsic theta rhythms using biophysical local field potential (LFP) models. *eNeuro*. 0146–18:2018.

Chen TW, Wardill TJ, Sun Y, Pulver SR, Renninger SL, Baohan A, Schreiter E, Kerr R, Orger M, Jayaraman V, et al. 2013. Ultrasensitive fluorescent proteins for imaging neuronal activity. *Nature*. 499:295–300.

David LS, Topolnik L. 2017. Target-specific alterations in the VIP inhibitory drive to hippocampal GABAergic cells after status epilepticus. *Exp Neurol*. 292:102–112.

Deneux T, Kaszas A, Szalay G, Katona G, Lakner T, Grinvald A, Rózsa B, Vanzetta I. 2016. Accurate spike estimation from noisy calcium signals for ultrafast three-dimensional imaging of large neuronal populations in vivo. *Nat Commun*. 7:12190.

Dombeck D, Harvey C, Tian L, Looger L, Tank D. 2010. Functional imaging of hippocampal place cells at cellular resolution during virtual navigation. *Nat Neurosci*. 13:1433–1440.

Dragoi G, Carpi D, Recce M, Csicsvari J, Buzsáki G. 1999. Interactions between hippocampus and medial septum during sharp waves and theta oscillation in the behaving rat. *J Neurosci*. 19:6191–6199.

Dudman J, Tsay D, Siegelbaum S. 2007. A role for synaptic inputs at distal dendrites: instructive signals for hippocampal long-term plasticity. *Neuron*. 56:866–879.

Ernst M, Brauchart D, Boresch S, Sieghart W. 2003. Comparative modeling of GABAA receptors: Limits, insights, future developments. *Neuroscience*. 119:933–943.

Francavilla R, Luo X, Magnin E, Tyan L, Topolnik L. 2015. Coordination of dendritic inhibition through local disinhibitory circuits. *Front Syn Neurosci*. 7:5.

Francavilla R, Villette V, Luo X, Chamberland S, Munoz-Pino E, Camiré O, Wagner K, Kis V, Somogyi P, Topolnik L. 2018. Connectivity and network state-dependent recruitment of long-range VIP-GABAergic neurons in the mouse hippocampus. *Nat Commun*. 9:5043.

Francavilla R, Villette V, Martel O, Topolnik L. 2019. Calcium dynamics in dendrites of hippocampal CA1 interneurons in awake mice. *Front Cell Neurosci*. 13:98.

Frerking M, Schulte J, Wiebe S, Stäubli U. 2005. Spike timing in CA3 pyramidal cells during behavior: Implications for synaptic transmission. *J Neurophysiol*. 94:1528–1540.

Gillies M, Traub R, LeBeau F, Davies C, Gloveli T, Buhl E, Whittington M. 2002. A model of atropine-resistant theta oscillations in rat hippocampal area CA1. *J Physiol*. 543:779–793.

Glickfeld LL, Scanziani M. 2006. Distinct timing in the activity of cannabinoid-sensitive and cannabinoid-insensitive basket cells. *Nat Neurosci*. 9:807–815.

Gloveli T, Dugladze T, Saha S, Monyer H, Heinemann U, Traub R, Whittington M, Buhl E. 2005. Differential involvement of oriens/pyramidaleinterneurones in hippocampal network oscillations in vitro. *J Physiol*. 562:131–147.

Golding N, Staff N, Spruston N. 2002. Dendritic spikes as a mechanism for cooperative long-term potentiation. *Nature*. 418:326–331.

Guet-McCreight A, Skinner F. 2019. Using computational models to predict in vivo synaptic inputs to interneuron specific 3 (IS3) cells of CA1 hippocampus that also allow their recruitment during rhythmic states. *Plos One*. 14:e0209429.

Guet-McCreight A, Camiré O, Topolnik L, Skinner F. 2016. Using a semi-automated strategy to develop multi- compartment models that predict biophysical properties of interneuron-specific 3 (IS3) cells in hippocampus. *eNeuro*. 3:4.

Gulyás A, Hájos N, Freund T. 1996. Interneurons containing calretinin are specialized to control other interneurons in the rat hippocampus. *J Neurosci*. 16:3397–3411.

Gulyás A, Megias M, Emri Z, Freund T. 1999. Total number and ratio of excitatory and inhibitory synapses converging onto single interneurons of different types in the CA1 area of the rat hippocampus. *J Neurosci*. 19:10082–10097.

Hangya B, Borhegyi Z, Szilágyi N, Freund T, Varga V. 2009. GABAergic neurons of the medial septum lead the hippocampal network during theta activity. *J Neurosci*. 29:8094–8102.

He M, Tucciarone J, Lee S, Nigro MJ, Kim Y, Levine JM, Kelly SM, Krugikov I, Wu P, Chen Y, et al. 2016. Strategies and tools for combinatorial targeting of GABAergic neurons in mouse cerebral cortex. *Neuron*. 91:1228–1243.

Jackson J, Ayzenshtat I, Karnani M, Yuste R. 2016. VIP+ interneurons control neocortical activity across brain states. *J Neurophysiol*. 115:3008–3017.

Jarsky T, Roxin A, Kath WL, Spruston N. 2005. Conditional dendritic spike propagation following distal synaptic activation of hippocampal CA1 pyramidal neurons. *Nat Neurosci*. 8:1667–1676.

Katona L, Lapray D, Viney TJ, Oulhaj A, Borhegyi Z, Micklem BR, Klausberger T, Somogyi P. 2014. Sleep and movement differentiates actions of two types of somatostatin-expressing GABAergic interneuron in rat hippocampus. *Neuron*. 82:872–886.

Klausberger T, Somogyi P. 2008. Neuronal diversity and temporal dynamics: The unity of hippocampal circuit operations. *Science*. 321:53–57.

Klausberger T, Magill PJ, Márton LF, Roberts JD, Cobden PM, Buzsáki G, Somogyi P. 2003. Brain-state- and cell-type-specific firing of hippocampal interneurons in vivo. *Nature*. 421:844–848.

Lapray D, Lasztoczi B, Lagler M, Viney TJ, Katona L, Valenti O, Hartwich K, Borhegyi Z, Somogyi P, Klausberger T. 2012. Behavior-dependent specialization of identified hippocampal interneurons. *Nat Neurosci*. 15:1265–1271.

Le Roux N, Cabezas C, Böhm UL, Poncer JC. 2013. Input-specific learning rules at excitatory synapses onto hippocampal parvalbumin-expressing interneurons. *J Physiol*. 591:1809–1822.

Leão RN, Mikulovic S, Leão KE, Munguba H, Gezelius H, Enjin A, Patra K, Eriksson A, Loew LM, Tort A, et al. 2012. OLM interneurons differentially modulate CA3 and entorhinal inputs to hippocampal CA1 neurons. *Nat Neurosci*. 15: 1524–1530.

Lee S, Hjerling-Leffler J, Zagha E, Fishell G, Rudy B. 2010. The largest group of superficial neocortical GABAergic interneurons expresses ionotropic serotonin receptors. *J Neurosci*. 30:16796–16808.

Lei S, McBain CJ. 2002. Distinct NMDA receptors provide differential modes of transmission at mossy fiber-interneuron synapses. *Neuron*. 33:921–933.

Losonczy A, Zhang L, Shigemoto R, Somogyi P, Nusser Z. 2002. Cell type dependence and variability in the short-term plasticity of EPSCs in identified mouse hippocampal interneurones. *J Physiol*. 542:193–210.

Lovett-Barron M, Turi G, Kaifosh P, Lee P, Bolze F, Sun X, Nicoud J, Zemelman B, Sternson S, Losonczy A. 2012. Regulation of

neuronal input transformations by tunable dendritic inhibition. *Nat Neurosci*. 15:423–430.

Luo X, Munoz E, Francavilla R, Vallee M, Droit A, Topolnik L. 2019. Transcriptomic profile of the subiculum-projecting VIP GABAergic neurons in the mouse CA1 hippocampus. *Brain Struct Funct*. 224:2269–2280.

Madisen L, Zwingman TA, Sunkin S, Oh S, Zariwala H, Gu H, Ng L, Palmiter R, Hawrylycz M, Jones A, et al. 2010. A robust and high-throughput Cre reporting and characterization system for the whole mouse brain. *Nat Neurosci*. 13:133–140.

Magee J, Cook EP. 2000. Somatic EPSP amplitude is independent of synapse location in hippocampal pyramidal neurons. *Nat Neurosci*. 3:895–903.

Magnin E, Francavilla F, Amalyan S, Gervais E, Luo X, David LS, Topolnik L. 2019. Input-specific synaptic location and function of the alpha5 GABAA receptor subunit in the mouse CA1 hippocampal neurons. *J Neurosci*. 39:788–801.

Malvache A, Reichinnek S, Villette V, Haimerl C, Cossart R. 2016. Awake hippocampal reactivations project onto orthogonal neuronal assemblies. *Science*. 353:1280–1283.

Masugi-Tokita M, Tarusawa E, Watanabe M, Molnár E, Fujimoto K, Shigemoto R. 2007. Number and density of AMPA receptors in individual synapses in the rat cerebellum as revealed by SDS-digested freeze-fracture replica Labeling. *J Neurosci*. 27:2135–2144.

Mikulovic S, Restrepo C, Siwani S, Bauer P, Pupe S, Tort A, Kullander K, Leão RN. 2018. Ventral hippocampal OLM cells control type 2 theta oscillations and response to predator odor. *Nat Commun*. 9:3638.

Mizuseki K, Sirota A, Pastalkova E, Buzsáki G. 2009. Theta oscillations provide temporal windows for local circuit computation in the entorhinal-hippocampal loop. *Neuron*. 64:267–280.

Nissen W, Szabo A, Somogyi I, Somogyi P, Lamsa K. 2010. Cell type-specific long-term plasticity at glutamatergic synapses onto hippocampal interneurons expressing either parvalbumin or CB1 cannabinoid receptor. *J Neurosci*. 30:1337–1347.

Nusser Z. 1999. A new approach to estimate the number, density and variability of receptors at central synapses. *Eur J Neurosci*. 11:745–752.

Nusser Z, Cull-Candy S, Farrant M. 1997. Differences in synaptic GABAA receptor number underlie variation in GABA mini amplitude. *Neuron*. 19:697–709.

Nyíri G, Stephenson FA, Freund T, Somogyi P. 2003. Large variability in synaptic n-methyl-d-aspartate receptor density on interneurons and a comparison with pyramidal-cell spines in the rat hippocampus. *Neuroscience*. 119:347–363.

Otmakhova N, Otmakhov N, Lisman J. 2002. Pathway-specific properties of AMPA and NMDA-mediated transmission in CA1 hippocampal pyramidal cells. *J Neurosci*. 22:1199–1207.

Pangalos M, Donoso JR, Winterer J, Zivkovic AR, Kempter R, Maier N, Schmitz D. 2013. Recruitment of oriens-lacunosum-moleculare interneurons during hippocampal ripples. *PNAS*. 110:4398–4403.

Papp E, Hájos N, Acsády L, Freund T. 1999. Medial septal and median raphe innervation of vasoactive intestinal polypeptide-containing interneurons in the hippocampus. *Neuroscience*. 90:369–382.

Paul A, Crow M, Raudales R, He M, Gillis J, Huang ZJ. 2017. Transcriptional architecture of synaptic communication delineates GABAergic Neuron identity. *Cell*. 171:522–539.

Pelkey KA, Chittajallu R, Craig MT, Tricoire L, Wester JC, McBain CJ. 2017. Hippocampal GABAergic inhibitory interneurons. *Physiol Rev*. 97:1619–1747.

Pi HJ, Hangya B, Kvitsiani D, Sanders J, Huang Z, Kepecs A. 2013. Cortical interneurons that specialize in disinhibitory control. *Nature*. 503:521–524.

Pinto L, Dan Y. 2015. Cell-type-specific activity in prefrontal cortex during goal-directed behavior. *Neuron*. 87:437–450.

Pouille F, Scanziani M. 2004. Routing of spike series by dynamic circuits in the hippocampus. *Nature*. 429:717–723.

Price C, Cauli B, Kovacs E, Kulik A, Lambolez B, Shigemoto R, Capogna M. 2005. Neurogliaform neurons form a novel inhibitory network in the hippocampal CA1 area. *J Neurosci*. 25:6775–6786.

Rahmati V, Kirmse K, Holthoff K, Kiebel SJ. 2018. Ultra-fast accurate reconstruction of spiking activity from calcium imaging data. *J Neurophysiol*. 119:1863–1878.

Royer S, Zemelman B, Losonczy A, Kim J, Chance F, Magee J, Buzsáki G. 2012. Control of timing, rate and bursts of hippocampal place cells by dendritic and somatic inhibition. *Nat Neurosci*. 15:769–775.

Rudy B, Fishell G, Lee S, Hjerling-Leffler J. 2011. Three groups of interneurons account for nearly 100% of neocortical GABAergic neurons. *Dev Neurobiol*. 71:45–61.

Salesse C, Lacharite-Mueller C, Chamberland S, Topolnik L. 2011. Age-dependent remodelling of inhibitory synapses onto hippocampal CA1 oriens-lacunosum moleculare interneurons. *J Physiol*. 589:4885–4901.

Sambandan S, Sauer JF, Vida I, Bartos M. 2010. Associative plasticity at excitatory synapses facilitates recruitment of fast-spiking interneurons in the dentate Gyrus. *J Neurosci*. 30:11826–11837.

Sik A, Penttonen M, Ylinen A, Buzsaki G. 1995. Hippocampal CA1 interneurons: An in vivo intracellular labeling study. *J Neurosci*. 15:6651–6665.

Siwani S, França A, Mikulovic S, Reis A, Hilscher M, Edwards S, Leão R, Tort A, Kullander K. 2018. OLMa2 cells bidirectionally modulate learning. *Neuron*. 99:404–412.

Sivagnanam S, Majumdar A, Yoshimoto K, Astakhov V, Bandrowski A, Martone M, Carnevale NT. 2013. Introducing The Neuroscience Gateway, Vol. 993 of CEUR Workshop Proceedings of CEUR Workshop Proceedings.

Soltesz I. 2006. *Diversity in the neuronal machine: Order and variability in interneuronal microcircuits*. Oxford, UK: Oxford University Press.

Somogyi J, Baude A, Omori Y, Shimizu H, El Mestikawy S, Fukaya M, Shigemoto R, Watanabe M, Somogyi P. 2004. GABAergic basket cells expressing cholecystokinin contain vesicular glutamate transporter type 3 (VGLUT3) in their synaptic terminals in hippocampus and isocortex of the rat. *Eur J Neurosci*. 19:552–569.

Spruston N, Jonas P, Sakmann B. 1995. Dendritic glutamate receptor channels in rat hippocampal CA3 and CA1 pyramidal neurons. *J Physiol*. 482:325–352.

Swanson G, Kamboj S, Cull-Candy S. 1997. Single-channel properties of recombinant AMPA receptors depend on RNA editing, splice variation, and subunit composition. *J Neurosci*. 17:58–69.

Szabo A, Somogyi J, Cauli B, Lambolez B, Somogyi P, Lamsa K. 2012. Calcium-permeable AMPA receptors provide a common mechanism for LTP in Glutamatergic synapses of distinct hippocampal interneuron types. *J Neurosci*. 32: 6511–6516.

Turi GF, et al. 2019. Vasoactive intestinal polypeptide-expressing interneurons in the hippocampus support goal-oriented spatial learning. *Neuron*. 101:1150–1165.

Tyan L, Chamberland S, Magnin E, Camiré O, Francavilla R, David LS, Deisseroth K, Topolnik L. 2014. Dendritic inhibition provided by interneuron-specific cells controls the firing rate and timing of the hippocampal feedback inhibitory circuitry. *J Neurosci*. 34:4534–4547.

Unal G, Joshi A, Viney T, Kis V, Somogyi P. 2015. Synaptic targets of medial septal projections in the hippocampus and extrahippocampal cortices of the mouse. *J Neurosci*. 35:15812–15826.

Varga C, Golshani P, Soltesz I. 2012. Frequency-invariant temporal ordering of interneuronal discharges during hippocampal oscillations in awake mice. *PNAS*. 109:2726–2734.

Villette V, Levesque M, Miled A, Gosselin B, Topolnik L. 2017. Simple platform for chronic imaging of hippocampal activity during spontaneous behaviour in an awake mouse. *Sci Rep*. 7:43388.

Viney T, Lasztoczi B, Katona L, Crump M, Tukker J, Klausberger T, Somogyi P. 2013. Network state-dependent inhibition of identified hippocampal CA3 axo-axonic cells in vivo. *Nat Neurosci*. 16:1802–1811.

Wang D, Yau H, Broker C, Tsou J, Bonci A, Ikemoto S. 2015. Mesopontine median raphe regulates hippocampal ripple oscillation and memory consolidation. *Nat Neurosci*. 18: 728–735.